Geophysical Journal International

Geophys. J. Int. (2014) **196,** 386–404
Advance Access publication 2013 October 15

doi: 10.1093/gji/ggt365

A comparison of approaches to the prediction of surface wave amplitude

Colleen A. Dalton,[1] Vala Hjörleifsdóttir[2] and Göran Ekström[3]

[1] *Department of Earth and Environment, Boston University, Boston, MA, USA. E-mail: dalton@bu.edu*
[2] *Departamento de Sismología, Instituto de Geofísica, Universidad Nacional Autónoma de México, México*
[3] *Lamont-Doherty Earth Observatory, Columbia University, Palisades, NY, USA*

Accepted 2013 September 10. Received 2013 August 19; in original form 2013 April 2

SUMMARY

A controlled experiment is performed to investigate how assumptions and simplifications in the measurement and analysis of surface wave amplitudes affect inferred attenuation variations in the mantle. Synthetic seismograms are generated using a spectral-element method for 42 earthquakes, 134 receiver locations and two earth models, both of which contain 3-D elastic properties and 1-D anelastic properties. Fundamental-mode Rayleigh-wave amplitudes are measured at periods of 50, 75 and 125 s for 4749 paths. The amplitudes are measured with respect to a reference waveform based on 1-D Earth structure, and thus amplitude observations that are not equal to unity can be attributed to differences in the computation of the spectral-element and reference waveforms or to uncertainties in the amplitude measurements themselves. Calculation of earthquake source excitation in the 3-D earth model versus the 1-D earth model has a significant effect on the amplitudes, especially at shorter periods, and variations in the average amplitude for each event are well explained by the effect of Earth structure at the event location on the source excitation. The effect of local Earth structure at the receiver location on the amplitude is, for most paths, much smaller than for the source amplitude. After correcting for source and receiver effects on amplitude, the remaining signal is compared to predictions of elastic focusing effects using the great-circle ray approximation, exact ray theory (ERT) and finite-frequency theory (FFT). We find that, for the earth models we have tested, ERT provides the best fit at 50 s, and FFT is most successful at 75 and 125 s, indicating that the broad zone of surface wave sensitivity cannot be neglected for the longer periods in our experiment. The bias introduced into attenuation models by focusing effects, which is assessed by inverting the measured amplitudes for 2-D attenuation maps, is most important at high spherical-harmonic degrees. Unaccounted-for scattering of seismic energy may slightly (<5 per cent) raise average global attenuation values at short periods but has no detectable effect at longer periods. The findings of this study also provide a set of guidelines for handling source, receiver and focusing effects that can be applied to surface wave amplitudes measured for the real Earth.

Key words: Surface waves and free oscillations; Seismic attenuation; Seismic tomography; Wave propagation.

1 INTRODUCTION

Surface wave amplitudes provide the best constraints available on the anelastic properties of the upper mantle (e.g. Mitchell 1995; Romanowicz 1995; Selby & Woodhouse 2002; Gung & Romanowicz 2004; Dalton & Ekström 2006a; Yang *et al.* 2007). However, surface wave amplitudes are influenced by factors in addition to attenuation, most notably excitation at the earthquake source, focusing and scattering by elastic heterogeneity during propagation, elastic structure at the receiver and the instrument response. The challenge of separating the signal of attenuation from the other factors that affect amplitudes is the primary reason that 3-D upper-mantle models of shear attenuation have not achieved the same resolution and degree of similarity that 3-D upper-mantle models of shear velocity have (e.g. Kustowski *et al.* 2008; Lekic & Romanowicz 2011; Ritsema *et al.* 2011). Seismic wave speed and attenuation have different and complementary sensitivites to temperature, composition, partial melt and volatiles (e.g. Hammond & Humphreys 2000; Lee 2003; Karato 2003; Faul & Jackson 2005), and therefore jointly interpreting these two sets of observations should help

improve and reduce some of the ambiguity in interpretations of wave speed (e.g. Roth *et al.* 2000; Yang *et al.* 2007; Dalton *et al.* 2009). Development of more accurate and higher resolution attenuation models is a necessary step for such interpretations to be possible.

In this paper, we use synthetic seismograms calculated with a spectral-element method to investigate the effects of source excitation, focusing and scattering and elastic structure at the receiver on surface wave amplitudes. We are particularly interested in understanding how approximate or incomplete treatment of these factors can introduce bias or errors into models of attenuation in the upper mantle. For example, Ferreira & Woodhouse (2007) demonstrated that the effect on amplitudes of the local Earth structure at the earthquake source can be similar in magnitude to the effect of elastic structure during propagation (focusing). Selby & Woodhouse (2000) and Dalton & Ekström (2006a) have shown how unmodelled focusing effects on Rayleigh-wave amplitudes can be mapped into attenuation anomalies on a global scale, especially for propagation through channels of low velocity such as mid-ocean ridges. Indeed, the treatment of focusing effects remains the primary obstacle for isolating the signal of attenuation in surface wave amplitude data.

The focusing effect on amplitude depends on the phase-velocity gradient perpendicular to the ray path, causing amplitudes to be especially sensitive to short-wavelength elastic structure and to errors in the assumed propagation path. For this reason, comparison of amplitudes due to focusing effects calculated with the great-circle ray approximation (GCRA), where the surface wave is treated as an infinitely thin ray confined to the great-circle path, and with exact ray theory (ERT), where the infinitely thin ray bends according to local velocity structure, shows stronger disagreement than the same comparison performed for phase delays (Wang & Dahlen 1994; Larson *et al.* 1998). These discrepancies are especially pronounced for longer paths, for which the deviation in the true ray path from the unperturbed great circle can be large. The validity of ray theory is limited to smooth heterogeneity with a length scale larger than the characteristic seismic wave wavelength; for rougher earth models or longer-period waves, it is necessary to consider the finite-frequency sensitivity of surface waves. Wang & Dahlen (1995) compared coupled-mode synthetic seismograms, which account for the finite Fresnel area of surface waves, with predictions of ERT for 150-s waves and found that agreement between the two approaches depended primarily on the wavelength of the assumed velocity model. A spherical-harmonic degree-12 model resulted in similar predictions of phase, amplitude and arrival angle; a degree-36 model led to weaker agreement, especially for amplitudes, and apparent overprediction of focusing effects with ray theory.

While there have been a number of recent efforts to compare ray theory and finite-frequency theory with forward and inverse approaches, the vast majority of these studies have been concerned with surface wave phase delays (e.g. Ritzwoller *et al.* 2002; Spetzler *et al.* 2002; Yoshizawa & Kennett 2004; Zhou *et al.* 2005; Boschi 2006; Bozdag & Trampert 2008). Considerably less attention has been paid to understanding how the different theoretical treatments for focusing affect wave amplitude and the implications of such differences for models of upper-mantle attenuation. The sensitivity of amplitudes to elastic heterogeneity through focusing effects extends their utility beyond studies of anelasticity; amplitudes provide a potentially valuable data set for constraining small-scale shear velocity structure. Dalton & Ekström (2006b) showed that Rayleigh-wave phase-velocity maps could be obtained from inversion of amplitude data alone, and joint inversion of phase and amplitude measurements for shear velocity models has been implemented in several recent studies (e.g. Yang *et al.* 2007; Dalton *et al.* 2008). A better understanding of the validity of different theoretical treatments for focusing effects can lead to improvements in both elastic and anelastic models.

To explore these and other issues, we have designed a controlled experiment to investigate the limits of several commonly used approaches to global surface wave tomography, with a particular focus on the use of fundamental-mode surface waves to map structure in the upper mantle. Synthetic seismograms were calculated using a spectral-element method for 42 earthquakes and two 3-D global earth models. Synthetic waveforms calculated in this way contain wave excitation and propagation effects that are often neglected or treated in an approximate fashion with typical surface wave measurement and inversion techniques. We seek to understand and quantify the extent to which surface wave observations can be meaningfully interpreted with ray-based approaches. Rayleigh-wave amplitudes are the subject of this paper. We evaluate how the earthquake source excitation, elastic structure at the receiver and focusing affect the amplitudes. In particular, we wish to identify potential sources of bias in existing attenuation models of the upper mantle. The analysis of phase delays measured from the synthetic seismograms will be considered in a future manuscript.

In Section 2, the experiment design and the measurement routine are described, and theoretical approaches to elastic focusing effects are reviewed. The results are presented in Section 3, and the implications of our results for global attenuation structure is explored in Section 4.

2 METHOD

Spectral-element synthetic seismograms were generated using the software package SPECFEM3D_GLOBE (Komatitsch & Tromp 2002a,b) for 42 globally distributed earthquakes and two different 3-D elastic global earth models. To isolate the effects of elastic structure on wave amplitudes, a 1-D attenuation model was used for all simulations. The earthquakes were selected from the Global CMT catalogue (Dziewonski *et al.* 1981; Ekström *et al.* 2012; www.globalcmt.org). The earthquakes are treated as point sources. These 42 events (Fig. 1) occurred during 2006–2007 and have magnitudes M_W 5.8–6.5 and depths <50 km. The earthquakes were selected to represent a variety of tectonic settings and focal mechanisms and to provide fairly even path coverage around the globe. To achieve a realistic station coverage, three-component

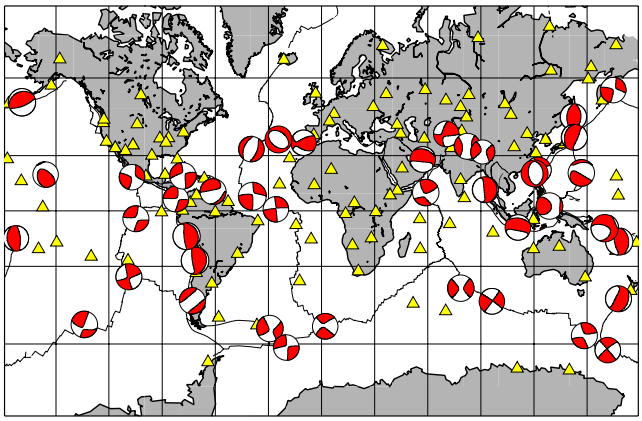

Figure 1. Location of 42 events and 134 stations (yellow triangles) for which SPECFEM synthetic seismograms were calculated.

seismograms were computed for 134 stations of the Global Seismographic Network (GSN) of the Incorporated Research Institutions for Seismology (IRIS) and the U.S. Geological Survey (USGS), and the GEOSCOPE network (network codes II, IU and G).

2.1 Earth models

Synthetic seismograms were calculated for two different 3-D global models of the elastic Earth structure, S362ANI (Kustowski *et al.* 2008) and MTS50. Model S362ANI (Fig. 2a) was developed through inversion of surface wave phase anomalies, long-period waveforms and body-wave traveltimes and contains variations in shear velocity relative to reference model STW105 (Kustowski *et al.* 2008) throughout the mantle. In the uppermost mantle, S362ANI is radially anisotropic. S362ANI is a relatively smooth model, parametrized horizontally with 362 spherical splines (approximately equivalent to spherical-harmonic degree 18).

In order to investigate the effects of the rougher Earth structure on surface waves, we created MTS50 (Fig. 2b), which is parametrized horizontally in spherical harmonics to degree 50. Degrees 0–18 of MTS50 are identical to S362ANI (Fig. 2c), and we have used the 3SMAC model (Nataf & Ricard 1996) to describe the smaller scale variations (degrees 19–50). 3SMAC is a 3-D earth model, defined on a $2^\circ \times 2^\circ$ grid, that was constructed not by inversion of seismic observations but rather from *a priori* assumptions about mantle temperature, chemistry and mineralogy. Defining MTS50 in this way allows for it to contain realistic small-scale structure such as subducting lithosphere and mantle plumes and for us to assess directly what is the influence of the higher degree anomalies on surface wave phase and amplitude, as differences between waveforms calculated with S362ANI and MTS50 will be primarily due to degrees 19–50 of MTS50.

The implementation of the earth models on the SPECFEM mesh utilizes 3-D crustal structure, including topography and water depth but not sediments, from CRUST2.0 (Bassin *et al.* 2000). Since the Moho depth in S362ANI and MTS50 is fixed at 24.4 km globally (Dziewonski & Anderson 1981), at locations where the Moho in CRUST2.0 is shallower than 24.4 km, the seismic properties of the uppermost mantle are extrapolated upwards to the base of the crust in the SPECFEM mesh. To isolate the effects of elastic structure on surface wave phase and amplitude, attenuation is allowed to vary only as a function of depth (Fig. 2d). The 1-D attenuation model used for these simulations is QL6 (Durek & Ekström 1996). Shear attenuation (Q_μ^{-1}) is 1/300 in the crust and 1/191 in the uppermost mantle (24.4–80.0 km). Variations in crustal thickness therefore lead to very slight lateral variations in attenuation near Moho depths.

We predict focusing effects on wave amplitude with various theoretical approximations using 2-D phase-velocity maps. The phase-velocity maps are calculated from the 3-D earth models using a local-mode approach (e.g. Tromp & Dahlen 1992). In practice, the Earth's surface is divided into $2^\circ \times 2^\circ$ pixels, and a 1-D earth model for each pixel is defined based on the seismic properties of the 3-D model at that location. A smoothing is applied to the crustal model to avoid artificial scattering and reflections from the boundaries between pixels. So that the phase-velocity maps are the most accurate representation of the earth model used for the SPECFEM simulations, the 1-D models are obtained by sampling the

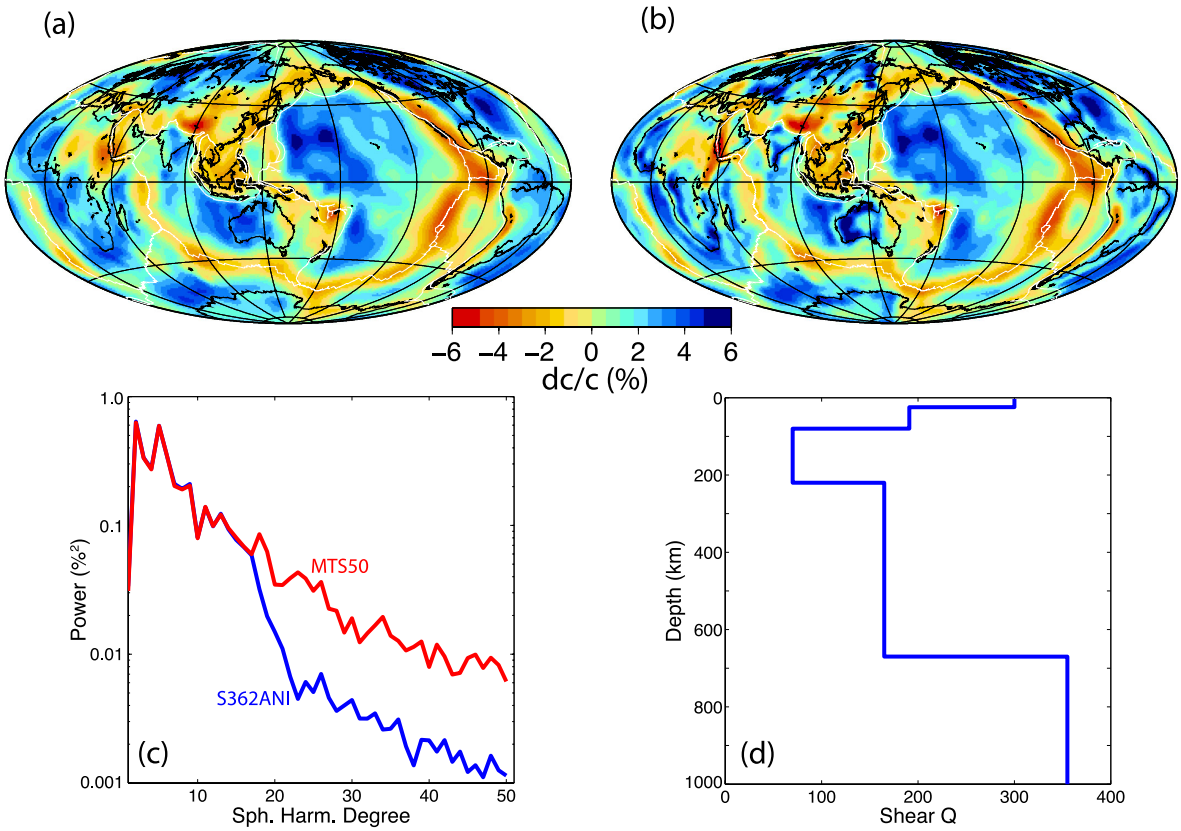

Figure 2. (a) Phase-velocity, calculated for earth model S362ANI, for 50-s Rayleigh waves. The map is expanded in spherical harmonics to degree 50. (b) As in (a) but for earth model MTS50. (c) Comparison of the power spectra of the two 50-s phase-velocity maps. (d) 1-D shear attenuation from model QL6 (Durek & Ekström 1996).

implementation of S362ANI or MTS50 on the SPECFEM mesh rather than the original model parametrizations in spherical harmonics or spherical splines. For each pixel, the local eigenfunctions, calculated for a spherically symmetric earth model whose properties are everywhere equal to the local structure, are determined using normal-mode theory, and the local surface wave slowness is calculated. The individual local slowness values are then combined to form global phase-velocity maps for each wave type and frequency (e.g. Figs 2a and b).

2.2 Amplitude measurements

The phase and amplitude of minor-arc fundamental-mode Rayleigh and Love waves in the SPECFEM synthetics are measured at periods between 50 and 125 s using the algorithm described by Ekström *et al.* (1997), which utilizes a phase-matched filter to isolate the fundamental mode from interfering overtones. The Rayleigh-wave amplitudes are the focus of this paper and will be referred to as 'measured', 'observed' or 'SPECFEM' amplitudes throughout the text. Under the assumption of ray theory on a sphere, a surface wave seismogram $u(\omega)$ can be written:

$$u(\omega) = A(\omega) \exp\left[\mathrm{i}\Phi(\omega)\right], \tag{1}$$

(e.g. Wang & Dahlen 1995; Ekström *et al.* 1997), where ω is the angular frequency, and the amplitude $A(\omega)$ and phase $\Phi(\omega)$ can be considered the product and sum, respectively, of three contributions:

$$A(\omega) = A_{\mathrm{S}}(\omega) A_{\mathrm{R}}(\omega) A_{\mathrm{P}}(\omega), \tag{2}$$

$$\Phi(\omega) = \Phi_{\mathrm{S}}(\omega) + \Phi_{\mathrm{R}}(\omega) + \Phi_{\mathrm{P}}(\omega). \tag{3}$$

The subscripts S, R and P denote the source, the receiver and the propagation path, respectively. The propagation amplitude $A_{\mathrm{P}}(\omega)$ includes geometrical spreading and focusing (A_{F}) and the decay due to attenuation (A_{Q}): $A_{\mathrm{P}}(\omega) = A_{\mathrm{F}}(\omega) A_{\mathrm{Q}}(\omega)$.

The surface waves in the SPECFEM synthetics are measured with respect to a reference seismogram that is generated by mode summation (Ekström *et al.* 1997). The reference waveform contains: source excitation, computed using the known earthquake location and focal mechanism and 1-D Earth elastic structure from PREM (Dziewonski & Anderson 1981); the receiver phase and amplitude, also calculated using the elastic Earth structure from PREM; and geometrical spreading and attenuation calculated for a spherically symmetric Earth. To be consistent with the SPECFEM synthetics, attenuation in the reference seismogram is calculated with QL6 (Durek & Ekström 1996). The theoretical reference waveform $u^0(\omega)$ can be written as

$$u^0(\omega) = A^0(\omega) \exp\left[\mathrm{i}\Phi^0(\omega)\right], \tag{4}$$

where

$$A^0(\omega) = A^0_{\mathrm{S}}(\omega) A^0_{\mathrm{R}}(\omega) A^0_{\mathrm{P}}(\omega). \tag{5}$$

The measured surface wave amplitude from the SPECFEM synthetics is therefore

$$\frac{A(\omega)}{A^0(\omega)} = \frac{A_{\mathrm{S}}(\omega)}{A^0_{\mathrm{S}}(\omega)} \frac{A_{\mathrm{R}}(\omega)}{A^0_{\mathrm{R}}(\omega)} \frac{A_{\mathrm{F}}(\omega)}{A^0_{\mathrm{F}}(\omega)} \frac{A_{\mathrm{Q}}(\omega)}{A^0_{\mathrm{Q}}(\omega)}, \tag{6}$$

where the two contributions to the propagation amplitude have been treated separately. Deviation of a measured amplitude anomaly away from unity reflects conditions at the source or receiver or along the propagation path that differ between the SPECFEM synthetic and the reference waveform. Such differences can originate from, for example:

(i) Differences in the calculation of source excitation in the synthetic seismograms, including assumptions about the local structure at the earthquake centroid location. Excitation is calculated in PREM for the reference waveform and in the 3-D earth model for the SPECFEM synthetic. Treatment of the source duration also differs for the two sets of calculations. In SPECFEM, the assumed source duration is determined from the half-duration of the Global CMT solution, and the shape of the source–time function is a Gaussian curve that best approximates a triangle with a width corresponding to twice the CMT half-duration. The reference waveform is calculated with a delta function source-time function. However, for the half-durations of the earthquakes in our data set (3.4–9.2 s) and the relatively long-period waves we are analysing (50–125 s), the effect of this difference on the amplitude measurements is much smaller than the effect of the local Earth structure at the source location.

(ii) Differences in the calculation of receiver amplitude owing to assumptions about the local Earth structure at the receiver location. Receiver amplitude is calculated in PREM for the reference waveform and in the 3-D earth model for the SPECFEM synthetic.

(iii) Focusing and defocusing by elastic heterogeneity during propagation. Because the reference waveform is calculated for a 1-D earth model, it does not contain focusing effects.

(iv) Waveform complexities, such as multiple scattering and multipathing, that are not included in the reference waveforms.

(v) Imperfect amplitude measurements owing to, for example, interference of overtones with the fundamental mode or complexities for paths located near a node in the source radiation pattern. The surface wave measurement routine utilized in this study (Ekström *et al.* 1997) contains several processing steps designed to minimize bias due to overtone interference. Nettles & Dziewonski (2011) demonstrated, using experiments with synthetic data, that the effect of overtone interference on Rayleigh-wave phase delays measured with this approach is small, and thus we expect that the effect of overtone interference on our Rayleigh-wave amplitudes is minor, especially relative to the other sources of bias in the amplitudes discussed below.

Non-unity measurements of amplitude cannot be attributed to attenuation structure, since the SPECFEM and reference waveforms are computed using the same 1-D attenuation model.

2.3 Focusing effects

One objective of this study is to assess various approximate theories for the treatment of focusing effects on surface wave amplitudes. We use the 2-D phase-velocity maps calculated from S362ANI and MTS50 to make predictions of focusing effects for each path and compare the predictions to the amplitudes measured from the SPECFEM synthetics; these comparisons are presented in Section 3. We consider three approximate theories: the GCRA and ERT, both of which treat the surface wave as a thin ray, and 2-D finite-frequency kernels that allow for a broad region of sensitivity surrounding the ray path.

2.3.1 Focusing prediction with the GCRA

In the case that heterogeneity is both smooth and slight (i.e. the phase-velocity perturbation $\frac{\delta c}{c_0}$ is small), the propagating surface wave may be treated using a line integral along the great circle

connecting the source and receiver (e.g. Woodhouse & Wong 1986; Wang & Dahlen 1994; Larson *et al.* 1998). We refer to this as 'GCRA'; it is also referred to as first-order ray-perturbation theory or the path-integral approximation in the literature. The amplitude anomaly due to focusing and defocusing along the ray path is given by

$$\log A_{\mathrm{F}}(\omega) = \frac{\delta c|_0}{2c_0}(\omega) + \frac{\delta c|_\Delta}{2c_0}(\omega) + \frac{1}{2}\mathrm{cosec}\Delta \times \int_0^\Delta \left[\sin(\Delta-\psi)\sin\psi\,\partial_\Theta^2 - \cos(\Delta-2\psi)\right]\frac{\delta c}{c_0}(\omega)\mathrm{d}\psi, \quad (7)$$

where Δ is the epicentral distance, ψ is the along-path coordinate, Θ is the path-perpendicular coordinate, $\frac{\delta c}{c_0}$ is the relative perturbation in surface wave phase velocity and $\delta c|_0$ and $\delta c|_\Delta$ indicate the phase-velocity perturbation at the source and receiver, respectively (e.g. Dahlen & Tromp 1998). In eq. (7), the amplitude due to focusing effects depends primarily on the second derivative of phase velocity perpendicular to the ray path.

2.3.2 Focusing prediction with ERT

If elastic heterogeneity is smooth and of a length scale larger than the characteristic seismic wave wavelength, it is sufficient to treat the surface wave as a thin ray. Expressions for calculating surface wave observables through ray tracing on a sphere can be found in the literature (e.g. Woodhouse & Wong 1986; Wang & Dahlen 1994; Larson *et al.* 1998). We refer to this as 'ERT'; it is also referred to as JWKB theory or ray theory in other studies. Wang & Dahlen (1995) compared ERT predictions of surface wave phase, amplitude and arrival angle with measurements from coupled-mode synthetic seismograms. They demonstrated, through statistical analysis of their measurements and theoretical considerations, that the validity of ERT can be assessed by the condition $\bar{s} \ll \sqrt{4\pi l}$, where $\bar{s}$, the rms degree of the phase-velocity map, is a measure of model roughness and l is the degree of the normal mode equivalent to the surface wave ($_nS_l$ or $_nT_l$ for spheroidal or toroidal modes, respectively). As period increases (l decreases), model roughness ($\bar{s}$) must be reduced in order for the condition to be met.

Because of their dependence on off-path velocity structure, amplitudes are especially sensitive to errors in the assumed propagation path. Wang & Dahlen (1994) and Larson *et al.* (1998) demonstrated through comparison of ERT and the GCRA that approximating the true ray path as the great-circle path is most accurate for predicting phase anomalies accumulated along short paths; disagreement is more significant for amplitudes and higher orbit surface waves, particularly when the magnitude of lateral velocity variations is large.

2.3.3 Focusing prediction with FFT

The true sensitivity of a seismic surface wave is distributed over a broad region surrounding the ray path. When the length scale of heterogeneity approaches the seismic wave wavelength, it is necessary to consider finite-frequency effects. We use the 2-D finite-frequency kernels of Zhou *et al.* (2004), which express the sensitivity of an amplitude measurement to perturbations in phase velocity. To obtain these 2-D kernels, 3-D finite-frequency kernels, which express the sensitivity of an amplitude measurement to perturbations in density, shear velocity and compressional velocity, are integrated radially. The integration requires making the forward-scattering approximation, which was shown by Zhou *et al.* (2004) to cause a slight enhancement of the sidebands in the kernels. Because of their relatively modest computational requirements, 2-D finite-frequency kernels are increasingly utilized in surface wave tomographic inversions (e.g. Yang & Forsyth 2006; Yoshizawa & Ekström 2010). For the forward calculations presented here, the 2-D kernels are integrated against the 2-D phase-velocity maps, which allows for a straightforward comparison with the ERT and GCRA focusing predictions.

With FFT, the amplitude due to focusing effects is related to the 2-D frequency-dependent phase velocity $\frac{\delta c}{c_0}(\omega,\theta,\phi)$ by

$$\log A_{\mathrm{F}}(\omega) = \int_\Omega K_A^c(\omega,\theta,\phi)\frac{\delta c}{c_0}(\omega,\theta,\phi)\mathrm{d}\Omega, \quad (8)$$

where integration is over the unit sphere Ω, and θ and ϕ are latitude and longitude, respectively. The quantity $K_A^c(\omega,\theta,\phi)$ is the 2-D single-frequency finite-frequency kernel for amplitude (Zhou *et al.* 2004),

$$K_A^c(\omega,\theta,\phi) = -\mathrm{Re}\left(\frac{2k^2 S' R'' \mathrm{e}^{-\mathrm{i}[k(\Delta'+\Delta''-\Delta)+\pi/4]}}{SR\sqrt{8\pi k|\sin\Delta'||\sin\Delta''|/|\sin\Delta|}}\right), \quad (9)$$

where k is the wavenumber, the single prime denotes the source-to-scatterer path, and the double prime denotes the scatterer-to-receiver leg. Path length along the great-circle path is given by Δ, and Δ' and Δ'' are the lengths of the source-to-scatterer and scatterer-to-receiver legs. Source-radiation and receiver-polarization factors are given by S and R, respectively.

Time-domain windowing and frequency averaging are inherent in our measurements of Rayleigh-wave amplitude. For consistency with the measurement routine, we use a frequency-averaged sensitivity kernel determined from a weighted average of single-frequency sensitivity kernels (eq. 9) in a frequency band of width $\Delta\omega = 0.029$ rad s^{-1} surrounding the centre frequency. In practice, 11 finite-frequency kernels are averaged for each path: one at the centre period, five at higher frequency and five at lower frequency. We also truncate the width of each kernel to exclude scatterers from which energy would arrive at the receiver outside of the measurement window.

In Section 3, we show predictions for two sets of finite-frequency kernels: those that account for the effect of the source radiation pattern on the scattered energy (FFT-SC) and those that do not, for which $S' = S$ in eq. (9) (FFT-NOSC). Fig. 3 presents a comparison of these sensitivities and illustrates the effect of the frequency averaging.

2.4 Comparison of observed and predicted amplitudes

In the following section, we present a comparison of observed amplitudes and amplitudes predicted due to focusing effects. We quantify the level of agreement between the two sets of amplitude anomalies using two measures: misfit and correlation coefficient. Here, misfit M is defined as

$$M = \frac{\sum_{i=1}^N \left|\log A_i^{\mathrm{obs}} - \log A_i^{\mathrm{pred}}\right|}{\sum_{i=1}^N \left|\log A_i^{\mathrm{obs}}\right|}, \quad (10)$$

where A_i^{obs} and A_i^{pred} are the observed and predicted amplitudes, respectively, and the sum is over the N paths in our data set. We choose the absolute value of the difference in amplitude anomalies rather than the squared difference so that the misfit is not overly skewed by outliers. We also calculate and report the correlation coefficient between the observed ($\log A_i^{\mathrm{obs}}$) and predicted ($\log A_i^{\mathrm{pred}}$) amplitude anomalies, because the amplitudes can be highly correlated but have

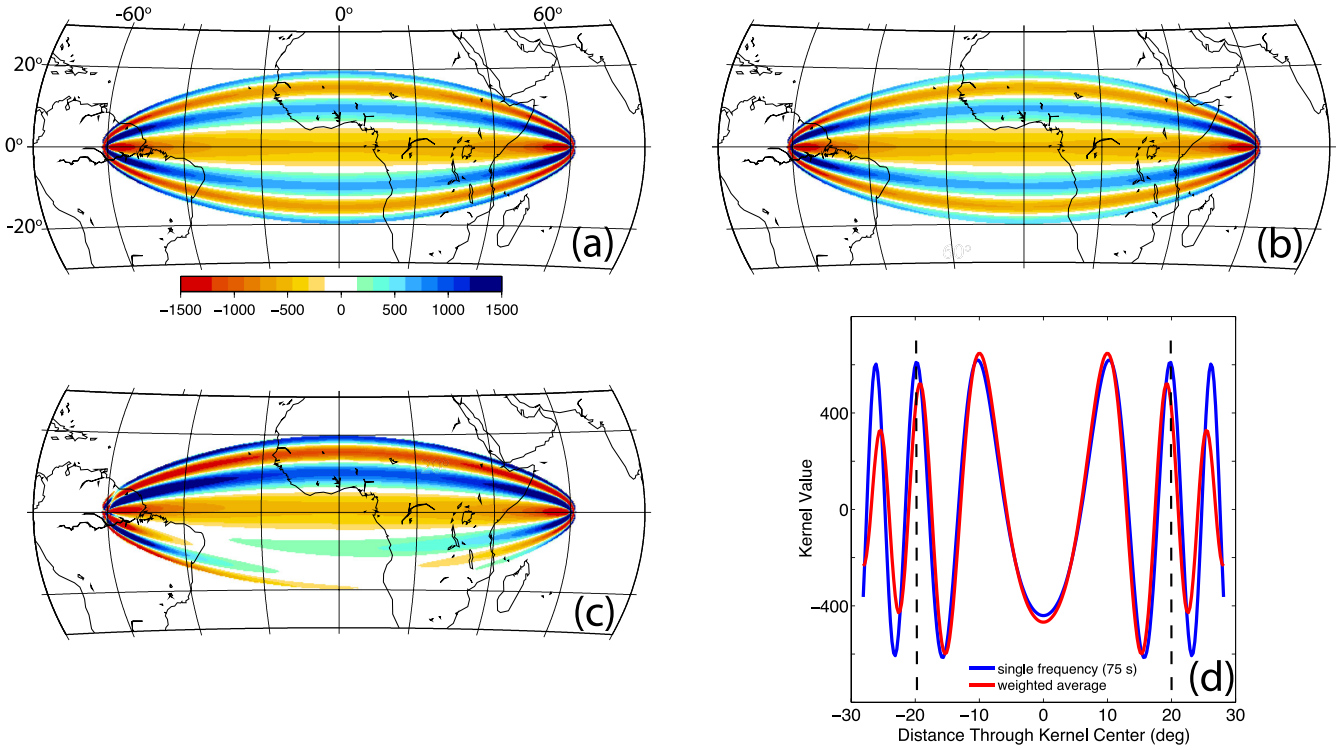

Figure 3. (a) Single-frequency finite-frequency kernel calculated for 75-s Rayleigh waves without the effects of the source radiation pattern. The epicentral distance is 119.3°, and the kernel has been rotated to the equator. This kernel describes the sensitivity of Rayleigh-wave amplitudes to phase-velocity perturbations (eq. 9). Values less than zero indicate that a negative phase-velocity perturbation ($\delta c/c < 0$) at that location contributes a positive amplitude anomaly. (b) Finite-frequency kernel that results from a weighted average of the 75-s sensitivity kernel with the kernels for 10 surrounding frequencies. (c) As in (a) but including the effects of the source radiation pattern. The maximum and minimum in the source radiation pattern are located ∼25° and 15°, respectively, away from the great-circle path for this particular event–station pair, enhancing the sidebands at positive latitudes and reducing them south of the equator in the coordinate system shown here. (d) Variation in finite-frequency sensitivity along the middle of the single-frequency and frequency-averaged kernels [i.e. variation along the line of longitude = 0° in (a) and (b)]. For the purposes of illustration, these curves are determined for wider kernels than shown in (a) and (b); the dashed lines indicate the width of the kernels in (a) and (b). The effect of frequency averaging on the kernel sidebands is especially apparent at distances >20° from the great-circle path and has a smaller effect for the kernel widths utilized in this paper (Section 2.3.3).

a large misfit value if the constant of proportionality between them is not ∼1.

3 RESULTS

The phase and amplitude of fundamental-mode Rayleigh waves are measured from the SPECFEM synthetics. Our data set consists of amplitudes for 4749 paths for simulations using S362ANI as the earth model and 4260 paths when MTS50 is the earth model. The data set is smaller than (number of earthquakes) × (number of stations) because the measurement routine rejects certain measurements for a variety of reasons, for example, if the dispersion curve is not smooth or if epicentral distance is <15° or >165° (Ekström *et al.* 1997). Furthermore, synthetic seismograms were calculated for fewer stations for MTS50 than S362ANI. Fig. 4 shows histograms of the amplitude measurements (i.e. eq. 6) at three periods. The median values, with S362ANI as the earth model, are 0.888, 0.948 and 0.945 at 50, 75 and 125 s, respectively. With MTS50, these median values are 0.889, 0.946 and 0.946. In all cases, 57–62 per cent of the measured amplitudes are <1, suggesting that for many paths the surface wave amplitudes in the normal-mode (reference) synthetics, with respect to which the measurements are made, are high relative to the SPECFEM synthetics. In the sections later, we explore the influence of the earthquake source, elastic structure at the receiver and focusing effects on the measured amplitudes. In Section 4, implications for the retrieved attenuation structure are discussed.

3.1 Effects of the earthquake source

In our experiment the earthquake source parameters are known perfectly, since they were prescribed for the computation of the SPECFEM synthetics. For the SPECFEM synthetics, source excitation occurs in the local Earth structure as specified by the 3-D earth model (S362ANI or MTS50, with crustal structure from CRUST2.0). For the reference waveforms, with respect to which the SPECFEM amplitude measurements are made, excitation occurs in PREM. In this section, we explore how the amplitude measurements are affected by the different assumptions about the Earth structure at the source location.

Fig. 5 shows the median value of all amplitude measurements available for each event in our data set, plotted at the centroid location. These event amplitudes vary with tectonic setting: lower-than-average amplitudes for mid-ocean-ridge earthquakes and higher amplitudes for events along subduction zones and in continental areas. Although the individual amplitude measurements contain source, propagation and receiver effects, examining the average amplitude for each event, which is typically determined from >115 observations, helps to emphasize the contribution of the sources to

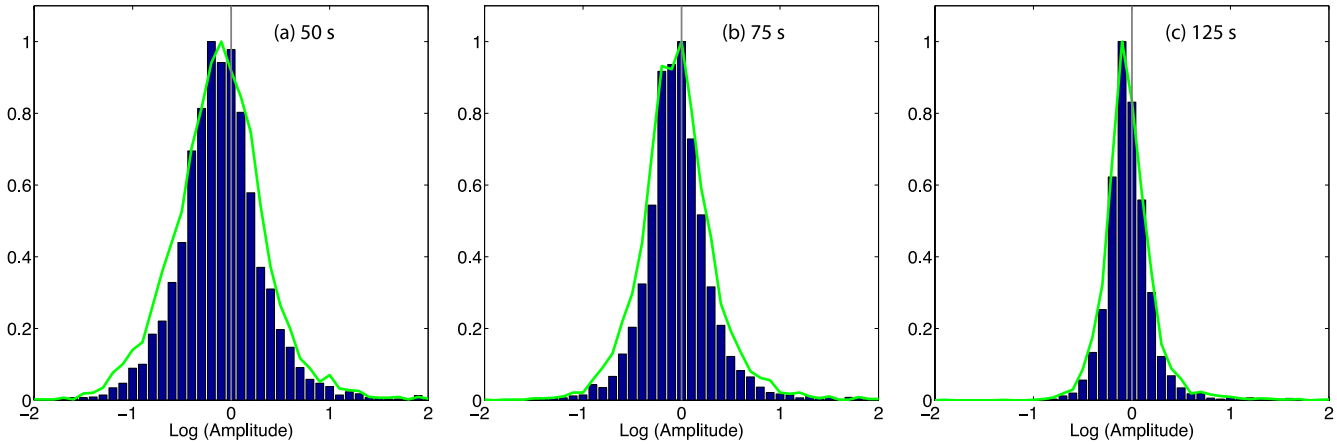

Figure 4. The distribution of measured amplitudes for 4749 paths measured with S362ANI as the earth model, normalized by the maximum value. The maximum value is 548, 737 and 1155 at 50, 75 and 125 s, respectively. Green curve shows the normalized distribution for the 4260 paths with MTS50 as the earth model; the maximum values are 427, 558 and 947. 'Amplitude' is the ratio of the amplitude in the SPECFEM synthetic to the amplitude in the reference waveform (i.e. eq. 6). The vertical line marks amplitude = 1.

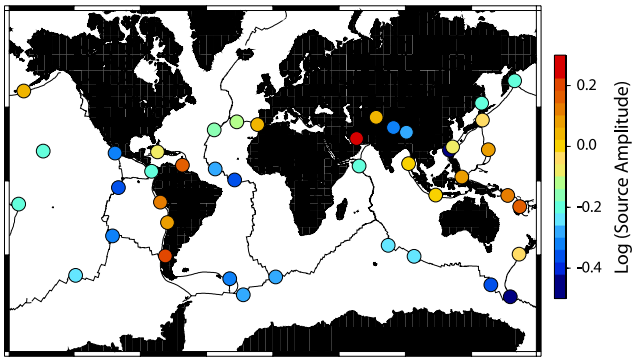

Figure 5. The median measured log(amplitude) for each event, for 50-s Rayleigh waves.

the amplitude data and de-emphasize the propagation and receiver contributions.

We can classify the 42 events in our data set by tectonic region using the GTR1 regionalization scheme (Jordan 1981). 20 of the earthquakes are located in an oceanic region: 12 beneath seafloor <25 Myr, six beneath seafloor 25–100 Myr and two beneath seafloor >100 Myr. The remaining 22 earthquakes are associated with Phanerozoic orogenic zones and magmatic belts on or near continents. The mean event amplitudes for the three oceanic regions are 0.747, 0.889 and 1.048 for 0–25, 25–100 and >100 Myr, respectively. The mean event amplitude for the 22 continental earthquakes is 0.930.

For each path in our data set, we predict the magnitude of source excitation in S362ANI and in PREM. Expressions for calculating the source excitation in terms of the radial eigenfunctions of a particular earth model and the moment–tensor components can be found in the literature, for example, Wang & Dahlen (1994), Zhou *et al.* (2004) and Ferreira & Woodhouse (2007). We sample S362ANI at the centroid location to determine the appropriate 1-D earth model for each event. Figs 6(a)–(c) show the ratio of these two source–excitation predictions. Values of the source–excitation ratio <1 indicate that excitation calculated in PREM is larger than excitation calculated in S362ANI. The histograms summarizing the source–excitation ratios contain two peaks, a feature that is especially clear at 50 s (Figs 6a–c). The two peaks are related to the tectonic classification of events described earlier: one group of paths, with small source–excitation ratios, that originate from earthquakes beneath young seafloor, and one group of paths from orogenic areas. This result is consistent with the findings of Abercrombie & Ekström (2003), who showed larger Rayleigh-wave excitation calculated in PREM, which has a 21-km-thick crust underlying a 3-km-thick water layer, relative to an earth model more representative of oceanic structure (5-km water layer, 6-km crust). These authors also showed that the excitation differences are most pronounced at short periods, in agreement with our results showing a larger spread of source–excitation ratios at shorter periods in Figs 6(a)–(c).

In Figs 6(d)–(f), the median predicted source–excitation ratio for each of the 42 events is compared to the median measured amplitude for each event. There is strong agreement between the two sets of values, indicating that some of the signal in the measured amplitudes can be explained by differences in the assumed Earth structure at the source in the SPECFEM synthetic (S362ANI) and the reference waveform (PREM). The diminished effect of source excitation at longer periods is apparent in both the smaller range of values spanned and the weaker correlation between measured amplitude and calculated source–excitation ratio. The correlation coefficient between the two sets of values is 0.94, 0.91 and 0.89 at 50, 75 and 125 s, respectively. The good agreement evident in Figs 6(d)–(f) also suggests that when working with amplitude data from the real Earth, for which the true Earth structure at the source is not perfectly known, the average amplitude for each event can be considered an effective proxy for the average source excitation when a sufficiently large number of stations is used.

3.2 Effects of the receiver

By analogy with the source excitation discussed, we can also calculate a 'receiver amplitude' for a 1-D earth model; expressions for the calculation of receiver amplitude can be found in, for example, Wang & Dahlen (1994) and Zhou *et al.* (2004). To explore how our amplitude measurements are affected by different assumptions about Earth structure at the receiver location, we calculate the receiver amplitude in PREM and in S362ANI for each path in our data set. We sample S362ANI at the receiver location to determine the appropriate 1-D earth model for each receiver. Figs 7(a)–(c) shows the ratio of these predicted receiver amplitudes. As compared to the source–excitation ratios (Figs 6a–c), these values are smaller, are

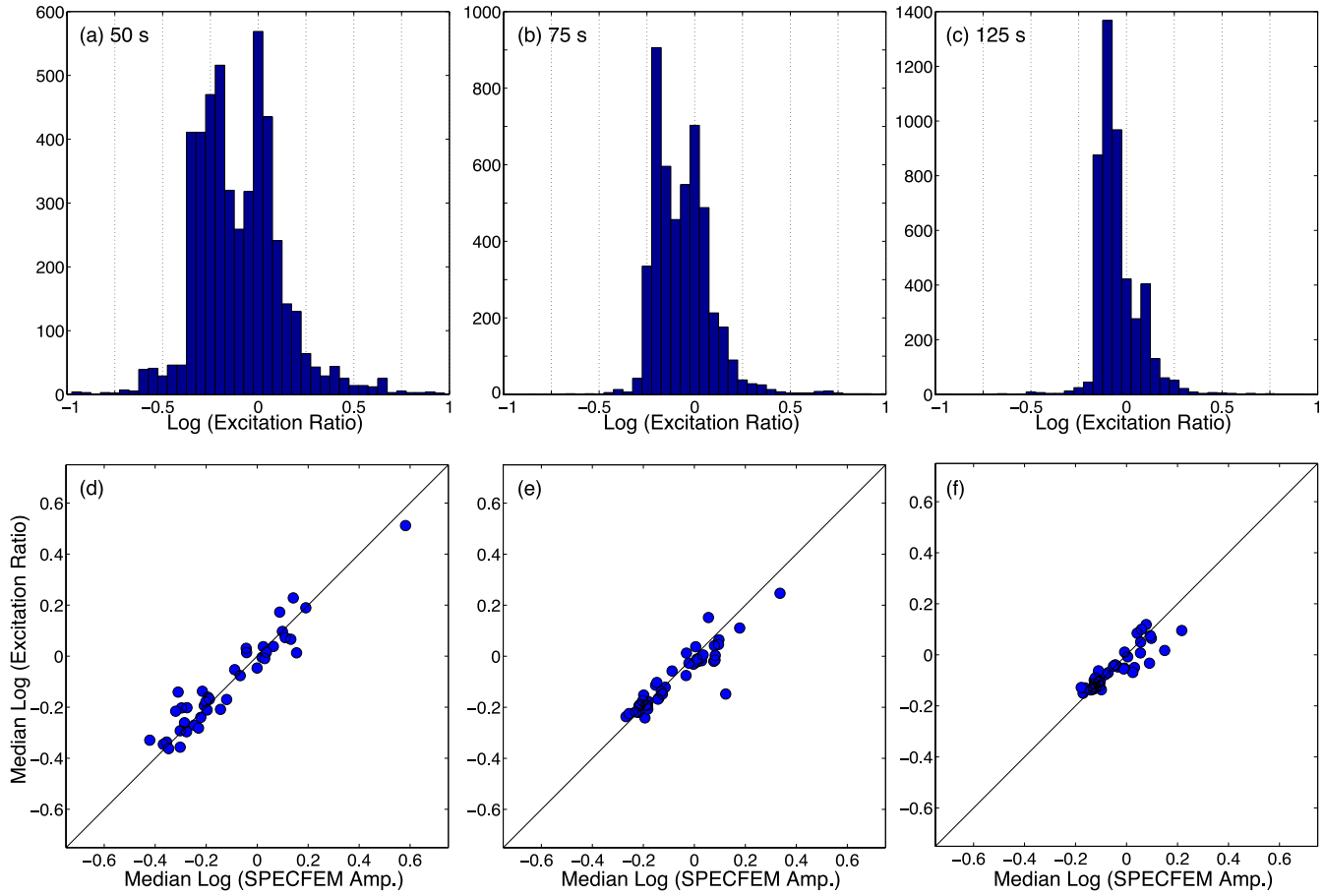

Figure 6. (a–c) Ratio of source excitation calculated in S362ANI to that calculated in PREM. The distribution of excitation ratios for 4749 paths is shown for three periods. (d–f) Comparison, for each event, of the median source–excitation ratio (vertical axis) and the median measured amplitude anomaly (horizontal axis).

more evenly distributed around zero and show weaker dependence on frequency.

For each receiver, the median measured amplitude is calculated and compared to the predicted receiver amplitudes in Figs 7(d)–(f). The 'measured' amplitudes in Fig. 7 have been corrected for source excitation using the source–excitation ratios described in Section 3.1. Agreement between the median amplitude measurement for each receiver and the predicted receiver–amplitude ratio is strongest at long periods: the correlation coefficient is 0.60, 0.71 and 0.81 at 50, 75 and 125 s, respectively. These correlations, while statistically significant, are smaller than those found for the source amplitudes. The median measured values in Fig. 7 are typically determined from 32–38 events, whereas the median measured values in Fig. 6 are typically determined from >115 stations. Furthermore, the effect on amplitude of the local Earth structure at the receiver is much smaller than for the local Earth structure at the source. Hence, the median amplitude measurement for each receiver is more likely to be influenced by path effects on amplitude, especially at shorter periods for which phase-velocity maps contain more heterogeneity, whereas such path effects are more effectively averaged out in the median amplitude measurement for each source.

The predicted receiver–amplitude ratios show a linear dependence on phase velocity, especially at longer periods (Figs 7d–f); the correlation coefficient between phase velocity and predicted receiver–amplitude ratio is -0.52, -0.89 and -0.94 at 50, 75 and 125 s. Since global variations in surface wave phase velocity are reasonably well known for the real Earth, this relationship suggests that it may be possible to account, in an approximate way, for the effect of the Earth structure at the receiver on real amplitude data using the relative phase velocity, especially at longer periods.

While the comparisons in Figs 7(d)–(f) address the influence of elastic structure at the receiver on Rayleigh-wave amplitudes, they do not address how errors in the instrument response influence the amplitude data. Systematic discrepancies between the reported and true instrument response have been identified at a number of global seismic stations (Ekström *et al.* 2006) and can have an effect on observed surface wave amplitudes that is considerably larger than the effect of elastic structure at the receiver.

3.3 Focusing and defocusing effects

3.3.1 S362ANI

Fig. 8 compares predictions of focusing effects for the S362ANI earth model, using the GCRA, ERT and finite-frequency theory without source-radiation effects (FFT-NOSC), with the measured amplitudes. In these figures, the measured amplitudes have been corrected for local structure at the source and receiver using the predicted source and receiver amplitudes described earlier. We consider the entire amplitude data set (4749 paths) and a subset of the full data set ('selected data set') for which paths located

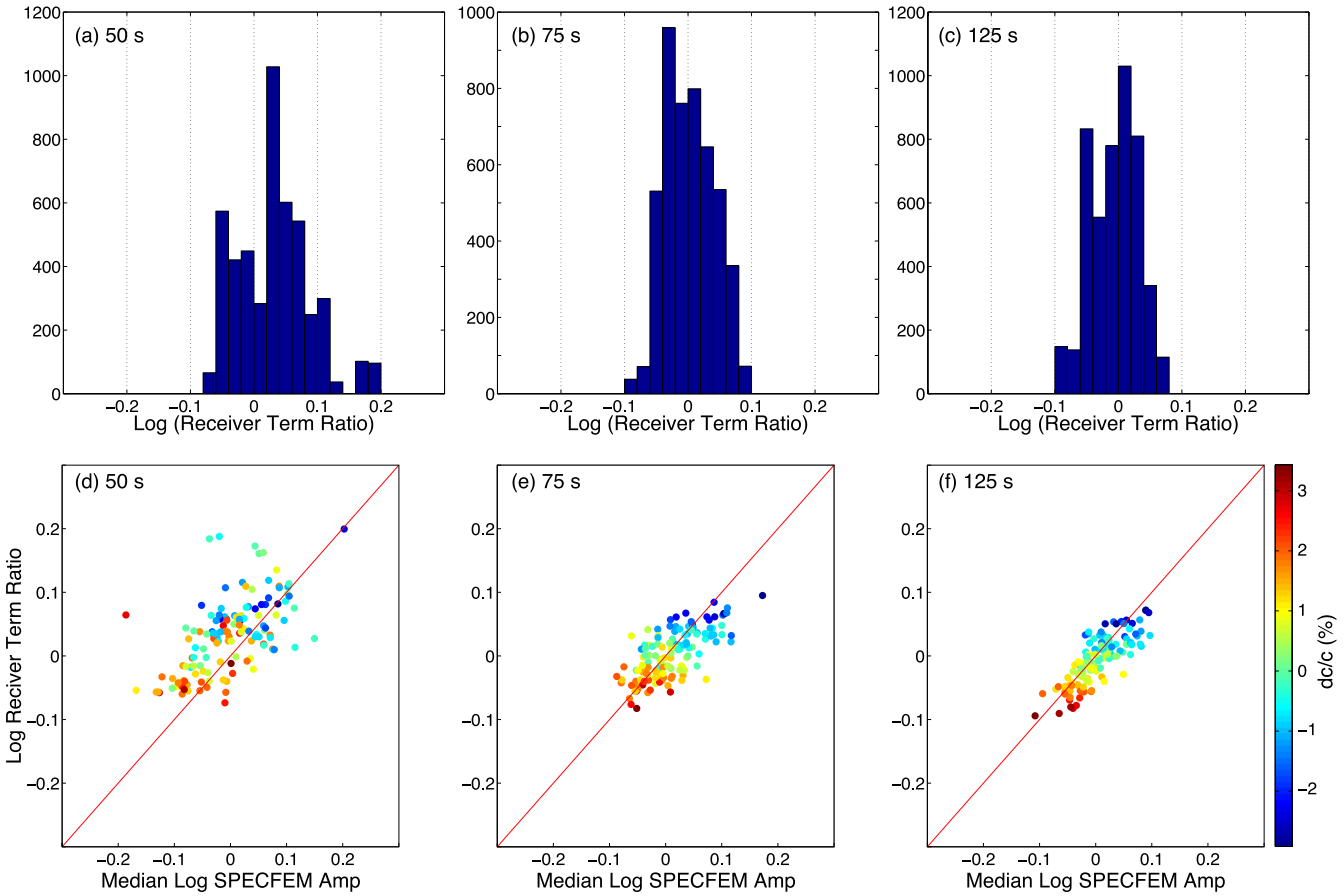

Figure 7. (a–c) Ratio of receiver amplitude calculated in S362ANI to that calculated in PREM. (d–f) Comparison, for each receiver, of the median measured amplitude anomaly corrected for source excitation (horizontal axis) and the receiver–amplitude ratio (vertical axis). The points are colour-coded by the value of Rayleigh-wave phase velocity (for S362ANI) at each receiver.

near a node in the earthquake radiation pattern are ignored (3234 paths). In the latter scenario, paths for which the calculated source amplitude is smaller than 0.5 times the maximum source amplitude for the corresponding event are excluded, which results in the elimination of 1515 amplitude measurements. Data selection by source amplitude does not affect the three sets of predictions, which depend only on phase velocity along the surface wave propagation path, but it may remove lower quality amplitude measurements for paths along which Rayleigh-wave excitation is relatively small.

Comparison of the measured and predicted amplitudes reveals a positive correlation for all three theoretical approximations. Correlation coefficients and misfit (eq. 10) are summarized in Table 1. At 50 s, ERT yields the lowest misfit value, and FFT-NOSC provides the highest correlation coefficient for the full data set. For the selected data set, ERT provides both the lowest misfit and the highest correlation. At longer periods (e.g. Fig. 9), FFT typically yields both the lowest misfit and the strongest correlation coefficient. FFT with source radiation included (FFT-SC) provides poor statistical fit to the measured data when all paths are considered (Table 1) because of some highly anomalous amplitude predictions near nodes in the radiation pattern. However, when only the selected data are considered, the correlation coefficient is dramatically improved. Focusing predictions with GCRA generally provide the poorest fit to the observations at all periods. Fig. 10(a) summarizes the comparison of observations and predictions for S362ANI.

The predicted amplitudes due to focusing effects show a stronger dependence on path length than the measured amplitudes do (Fig. 11a). For small epicentral distances ($<70^\circ$), the theoretical approximations yield a smaller range of amplitudes than measured. At intermediate distances (70°–110°), the observations and predictions exhibit a similar range of amplitude values. For the longest paths, most of the predictions result in a larger range of amplitudes than observed, especially for GCRA. This dependence on distance is not apparent in Fig. 8; Figs 11(b)–(d) show the comparison of measured and GCRA-predicted amplitudes in three distance bins containing equal numbers of paths. For short paths, GCRA underpredicts amplitudes, and for long paths, GCRA overpredicts focusing effects. For intermediate-length paths, the range of amplitudes spanned is roughly equivalent.

Consideration of the influence of path length introduces some subtleties into the interpretation of misfit and correlation coefficient (Fig. 12). For example, for short paths GCRA and ERT provide a similar level of misfit to the amplitude measurements at 50 s; the poor misfit obtained by GCRA for the longest paths is a significant contributor to the overall large misfit of GCRA when the full data set is considered together (Fig. 10a). It is also clear that at 75 s, FFT-NOSC yields the lowest misfit for intermediate and long paths, resulting in the lowest misfit for the full data set, but that for short paths ERT and GCRA provide the lowest misfit. Thus, the conclusions drawn from Fig. 10(a)—that ERT most successfully predicts focusing effects at 50 s and FFT most successfully predicts

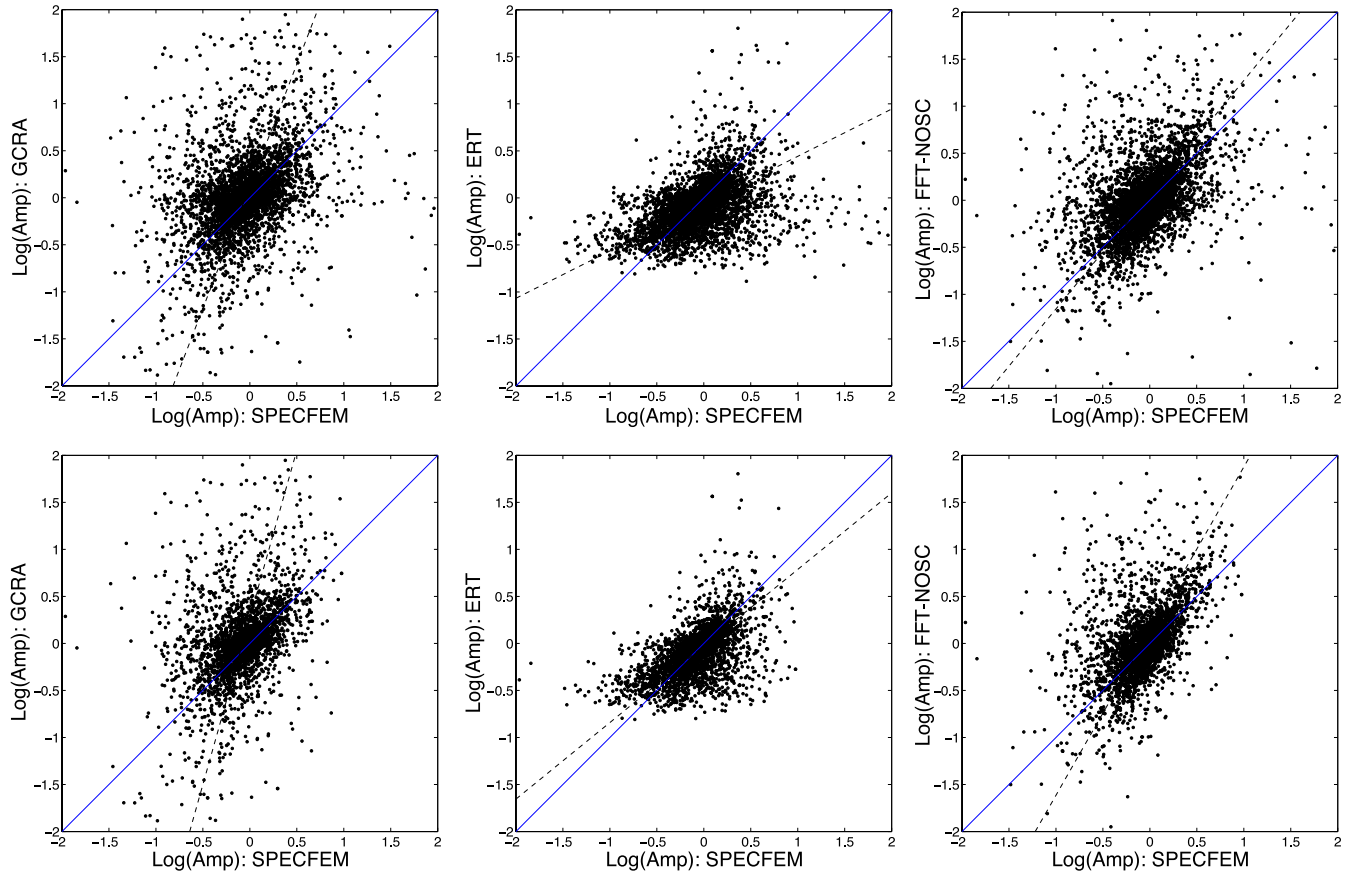

Figure 8. For 50-s Rayleigh waves. (Top row) Comparison of measured (SPECFEM) and predicted amplitude anomaly for all 4749 paths. Predictions are made using the great-circle ray approximation (GCRA), exact ray theory (ERT) and finite-frequency theory that does not account for source radiation (FFT-NOSC). Phase-velocity map for S362ANI was used for the predictions. Black dashed line is the best-fitting line, calculated with orthogonal regression. (Bottom row) As above, but here the comparison is performed for the 3234 paths selected for being away from nodes in the source radiation pattern.

Table 1. Summary of the degree of agreement between measured amplitude anomalies and focusing effects predicted by the great-circle ray approximation (GCRA), exact ray theory (ERT), finite-frequency theory that does not account for source radiation (FFT-NOSC), and finite-frequency theory that does account for source radiation (FFT-SC). The table reports misfit (eq. 10) and the correlation coefficient between measured and predicted amplitude anomalies. Values are tabulated for S362ANI and MTS50 for 'all paths' in the data set (4749 paths for S362ANI and 4260 paths for MTS50) as well as for 'selected paths' that are away from nodes in the radiation pattern (∼3100 for S362ANI and ∼2800 for MTS50). Values in parentheses report statistics calculated for the overlapping path coverage for S362ANI and MTS50 (see text).

	S362ANI				MTS50			
	All paths		Selected paths		All paths		Selected paths	
	Misfit	Corr. coeff.	Misfit	Corr. coeff.	Misfit	Corr. coeff.	Misfit	Corr. coeff.
50 s	$N = 4749$ (3232)		$N = 3234$ (2244)		$N = 4260$ (3232)		$N = 2938$ (2244)	
GCRA	1.20 (1.20)	0.28 (0.29)	1.28 (1.29)	0.32 (0.29)	1.61 (1.60)	0.20 (0.21)	1.70 (1.67)	0.22 (0.24)
ERT	0.91 (0.91)	0.38 (0.40)	0.84 (0.86)	0.51 (0.51)	0.98 (0.97)	0.33 (0.35)	0.92 (0.91)	0.43 (0.43)
FFT-NOSC	1.03 (1.03)	0.42 (0.44)	1.07 (1.09)	0.46 (0.45)	1.06 (1.07)	0.41 (0.42)	1.09 (1.10)	0.45 (0.44)
FFT-SC	1.61 (1.57)	0.17 (0.18)	1.32 (1.34)	0.47 (0.46)	1.57 (1.53)	0.12 (0.22)	1.32 (1.32)	0.46 (0.46)
75 s	$N = 4749$ (3232)		$N = 3097$ (2159)		$N = 4260$ (3232)		$N = 2821$ (2159)	
GCRA	1.10 (1.10)	0.35 (0.38)	1.17 (1.17)	0.44 (0.43)	1.76 (1.74)	0.17 (0.16)	1.89 (1.83)	0.25 (0.25)
ERT	1.02 (1.03)	0.27 (0.29)	0.98 (0.99)	0.43 (0.45)	1.22 (1.22)	0.20 (0.22)	1.20 (1.21)	0.33 (0.34)
FFT-NOSC	0.87 (0.87)	0.48 (0.51)	0.82 (0.84)	0.61 (0.60)	0.87 (0.85)	0.47 (0.50)	0.82 (0.80)	0.59 (0.59)
FFT-SC	1.25 (1.20)	0.11 (0.22)	0.97 (1.00)	0.64 (0.65)	1.21 (1.17)	0.14 (0.23)	0.96 (0.95)	0.61 (0.62)
125 s	$N = 4749$ (3232)		$N = 3028$ (2116)		$N = 4260$ (3232)		$N = 2744$ (2116)	
GCRA	1.26 (1.27)	0.24 (0.27)	1.44 (1.47)	0.33 (0.35)	2.23 (2.22)	0.11 (0.10)	2.69 (2.61)	0.19 (0.18)
ERT	1.18 (1.20)	0.18 (0.18)	1.25 (1.27)	0.32 (0.34)	1.58 (1.61)	0.16 (0.18)	1.75 (1.79)	0.32 (0.30)
FFT-NOSC	0.83 (0.82)	0.38 (0.41)	0.75 (0.74)	0.57 (0.62)	0.81 (0.80)	0.40 (0.44)	0.72 (0.71)	0.67 (0.67)
FFT-SC	1.00 (0.96)	0.02 (0.10)	0.80 (0.80)	0.61 (0.67)	0.99 (0.94)	0.17 (0.24)	0.80 (0.79)	0.67 (0.67)

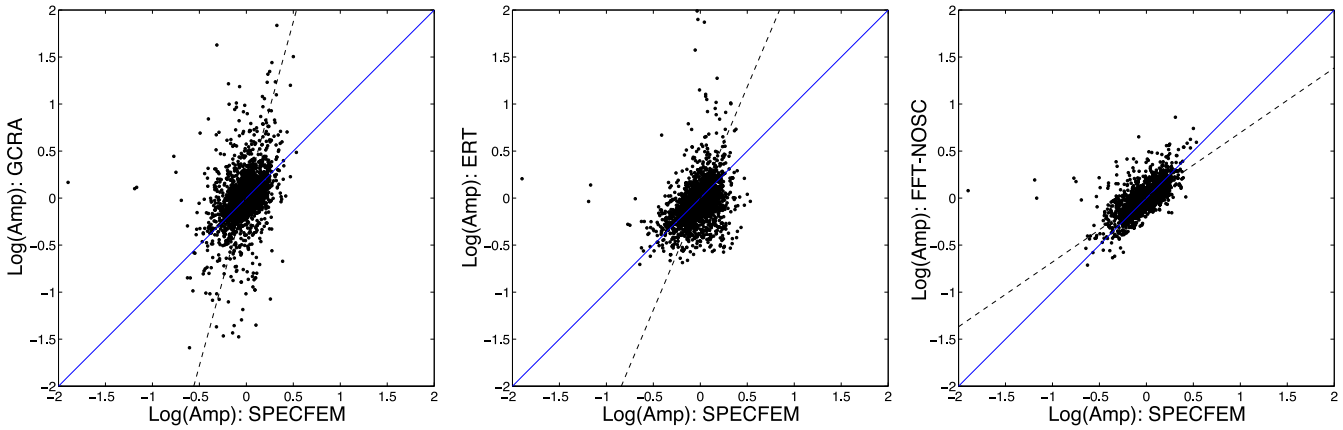

Figure 9. For 125-s Rayleigh waves. As in bottom row of Fig. 8: comparison of measured (SPECFEM) and predicted amplitude anomaly for 3028 paths selected for being away from nodes in the source radiation pattern.

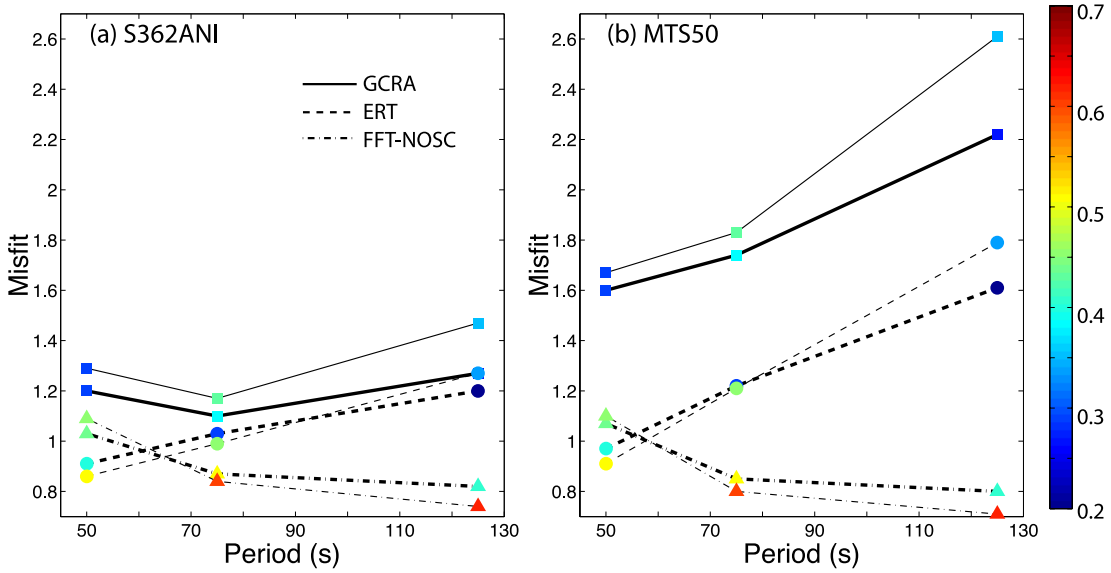

Figure 10. Summary of misfit for (a) S362ANI and (b) MTS50. Squares: GCRA; circles: ERT; triangles: FFT-NOSC. Points are colour-coded by correlation coefficient. Thick lines correspond to all paths shared in common by S362ANI and MTS50; thin lines correspond to paths selected for being away from nodes in the source radiation pattern.

focusing effects at 75 and 125 s—require refinement when path length is considered.

3.3.2 *MTS50*

Table 1 and Fig. 10(b) summarize the misfit between measured amplitudes that have been corrected for local source and receiver structure and focusing-predicted amplitudes for the MTS50 earth model. Since there is not identical path coverage for the S362ANI and MTS50 simulations, the misfit values shown in Fig. 10 are calculated using only the common paths (3232 for all paths and ∼2200 for selected paths). Table 1 also provides misfit values determined for the full data set; the conclusions remain the same regardless of whether the full set of paths or the overlapping set of paths is considered.

The results are in general agreement with the findings for S362ANI. At short periods (50 s), ERT provides the best fit to the measured amplitudes, and at longer periods FFT-NOSC is most successful. As compared to the results for S362ANI, there are larger differences between the misfit calculated for the three theoretical approximations. For example, GCRA and ERT provide a roughly similar level of misfit to the measurements for S362ANI at 75 and 125 s (Fig. 10a), whereas GCRA provides a very poor fit to the measurements at all periods for MTS50. The difference in misfit between ERT and FFT-NOSC is also much larger at 75 and 125 s for MTS50 than it is for S362ANI. Since the length-scale of heterogeneity in MTS50 is smaller than in S362ANI, ERT is a less-useful approximation in MTS50 at 75 and 125 s.

Fig. 13 provides a comparison of the magnitudes of the source, receiver and focusing effects on Rayleigh-wave amplitude. The median of the absolute value of the logarithm of the amplitudes calculated for the source–excitation ratio, the receiver–amplitude ratio, and focusing effects predicted with GCRA and FFT-NOSC are compared for S362ANI (4749 paths) and MTS50 (4260 paths). For S362ANI, the effect of the local Earth structure on the excitation ratio is the largest contributor to the total wave amplitude at all periods, although focusing predicted with FFT-NOSC and GCRA is only slightly smaller. For MTS50, the focusing predictions are the largest contributor to amplitude, followed by the source–excitation ratio. The effect of elastic structure at the receiver location on

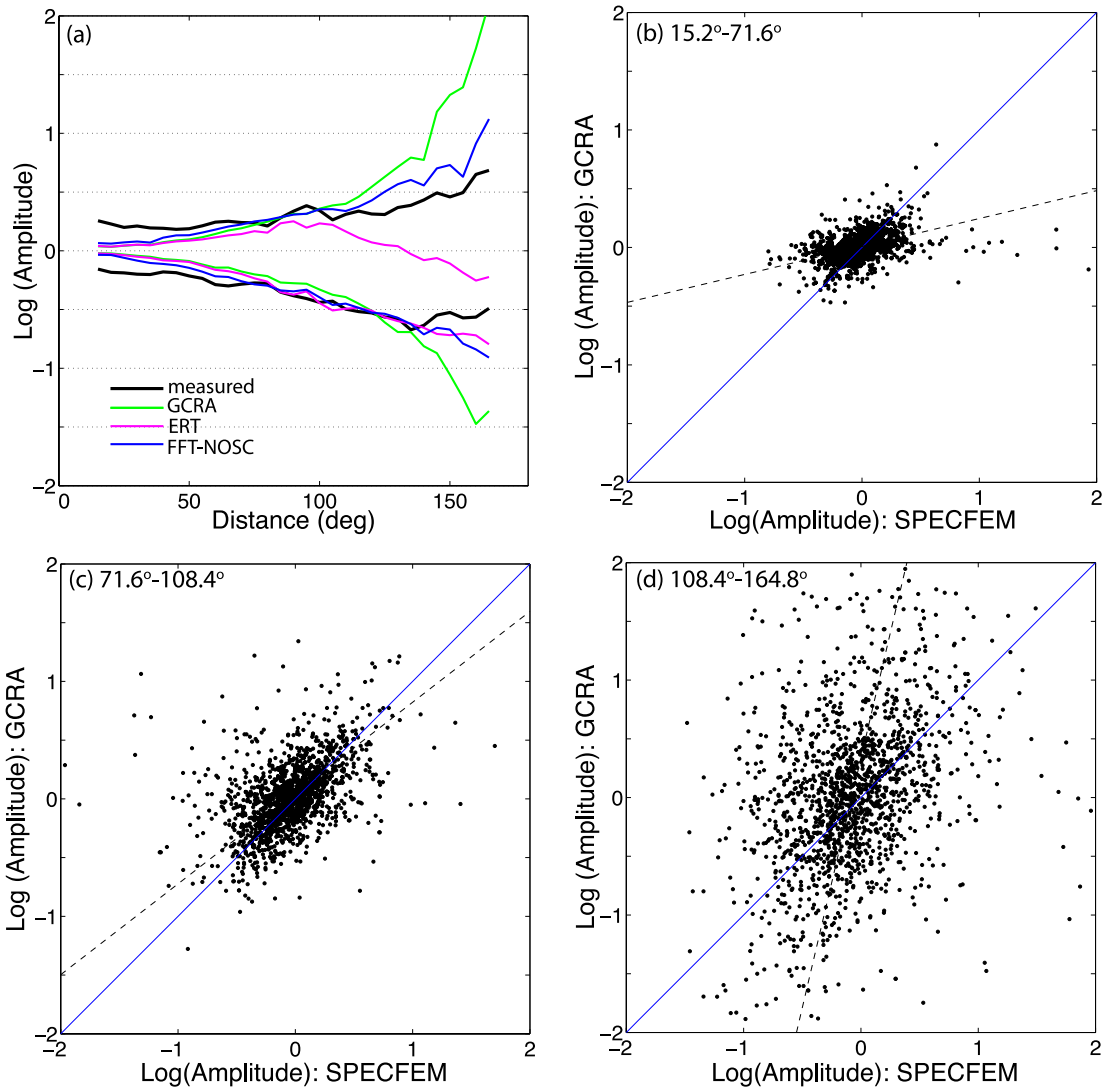

Figure 11. For 50-s Rayleigh waves. (a) Spread of amplitudes as a function of epicentral distance. Envelope encloses the median ± one standard deviation of the measured and predicted amplitude anomalies. (b) Comparison of measured amplitudes and amplitudes predicted using GCRA for 1583 paths with $15.2° \leq \Delta \leq 71.6°$. (c) As in (b) but for 1583 paths with $71.6° \leq \Delta \leq 108.4°$. (d) As in (b) but for 1583 paths with $108.4° \leq \Delta \leq 164.8°$. Black dashed line is the best-fitting line, calculated with orthogonal regression.

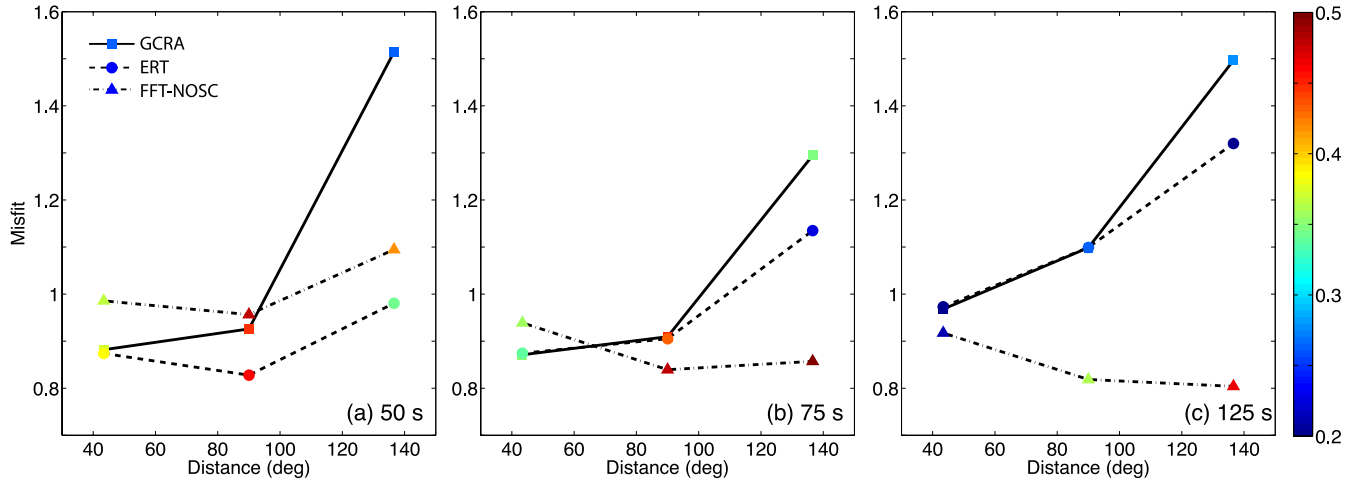

Figure 12. Misfit calculated separately for three distance bins and plotted at the centre of each bin: $\Delta = 15.2°–71.6°$, $\Delta = 71.6°–108.4°$ and $\Delta = 108.4°–164.8°$. Colour-coded by correlation coefficient. Each distance bin contains 1583 paths. The S362ANI earth model was used for these measurements and predictions.

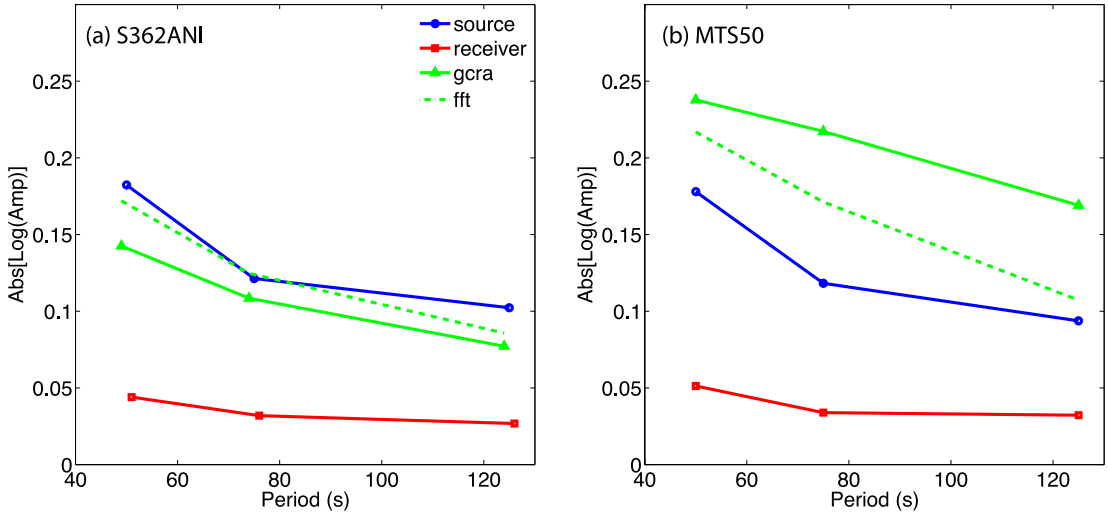

Figure 13. Median of the absolute value of the different contributions to Rayleigh-wave amplitude, determined using all paths. Blue: source excitation ratio; red: Receiver–amplitude ratio; solid green: focusing predictions with GCRA; dashed green: focusing predictions with FFT-NOSC. (a) S362ANI and (b) MTS50.

amplitude is much smaller than the source or focusing effects for both S362ANI and MTS50 at all periods. The source and receiver contributions have similar magnitudes for S362ANI and MTS50. However, the magnitude of the focusing predictions is much larger for MTS50, reflecting the dependence of focusing amplitude on the roughness of the earth model.

4 DISCUSSION

4.1 Implications for attenuation maps

We are interested in understanding the ways in which unmodelled source, receiver and path effects on surface wave amplitude can be mapped into erroneous attenuation structure. Here, we consider this issue from two different angles. In the first case, we exploit the fact that we know the earthquake source parameters and the 3-D Earth structure in our experiment perfectly, and thus the effects of the local Earth structure on source excitation and receiver amplitude can be precisely accounted for. The remaining signal in the amplitudes can then be used to investigate how focusing and scattering influence the attenuation structure. In the second case, we replicate the conditions of the real Earth, for which we have imperfect knowledge of the Earth structure and earthquake parameters. We follow the approach of Dalton & Ekström (2006a) and invert the amplitude measurements for source correction factors, receiver correction factors and attenuation structure using the GCRA. With this approach we can assess how well the source and receiver correction factors capture the true variations in source and receiver amplitude and how unmodelled focusing and scattering effects are mapped into attenuation anomalies. The SPECFEM amplitudes calculated for the S362ANI model are used for all investigations described in this section.

4.1.1 Scenario 1: perfectly known source parameters and the Earth structure

Fig. 14(a) shows the attenuation map that is obtained when the raw amplitude measurements for 4749 paths are inverted for variations in attenuation. The amplitude measurements $A(\omega)$ are related to attenuation anomalies along the ray path connecting source S and receiver R via

$$A(\omega) = \exp\left[-\frac{\omega}{2\,U(\omega)}\int_S^R \delta Q^{-1}(\omega,\theta,\phi)\mathrm{d}s\right], \qquad (11)$$

where $U(\omega)$ is the group velocity and $\delta Q^{-1}(\omega, \theta, \phi)$ is the perturbation in attenuation at latitude θ and longitude ϕ. The ray path is approximated by the great-circle path and the maps are expanded in spherical harmonics to degree 12. In Fig. 14(c), the maps are determined from the 3234 paths selected for being away from nodes in the radiation pattern. The median measured amplitude for each event is plotted on top of the attenuation variations to illustrate how the differences in source excitation, when not accounted for, result in prominent attenuation anomalies centred on the earthquake location.

Figs 14(b) and (d) show the attenuation variations obtained when the raw amplitude measurements have been corrected for local source and receiver structure. The heterogeneity is smaller than in Figs 14(a) and (c), and the clear association between attenuation anomalies and earthquake locations has disappeared, but considerable variations remain, perhaps most notably the linear zones of low attenuation along mid-ocean ridges. The variance reduction provided by these maps is relatively small, ∼15–20 per cent (Fig. 16b).

We explore whether Figs 14(b) and (d) contain signal due to focusing effects, which have not been accounted for, by comparing them to the attenuation maps obtained when the predicted amplitudes due to focusing effects are attributed entirely to attenuation (Fig. 15). Amplitudes predicted with GCRA, ERT and FFT-NOSC are considered separately. There are clearly similarities between the patterns in Fig. 15 and the patterns in Figs 14(b) and (d). For the maps determined from only the selected paths, the correlation coefficient with the maps in Fig. 15 is highest for ERT at 50 s and for FFT-NOSC at longer periods (Fig. 16a), consistent with the results in Fig. 10(a). For the maps determined from all paths, correlation is highest for GCRA at all periods. The attenuation maps derived from the GCRA and ERT focusing-predicted amplitudes (i.e. Figs 15a and b) provide a small amount of variance reduction for the amplitude measurements (Fig. 16b). The maps derived from the FFT-predicted amplitudes provide a relatively poor fit to the

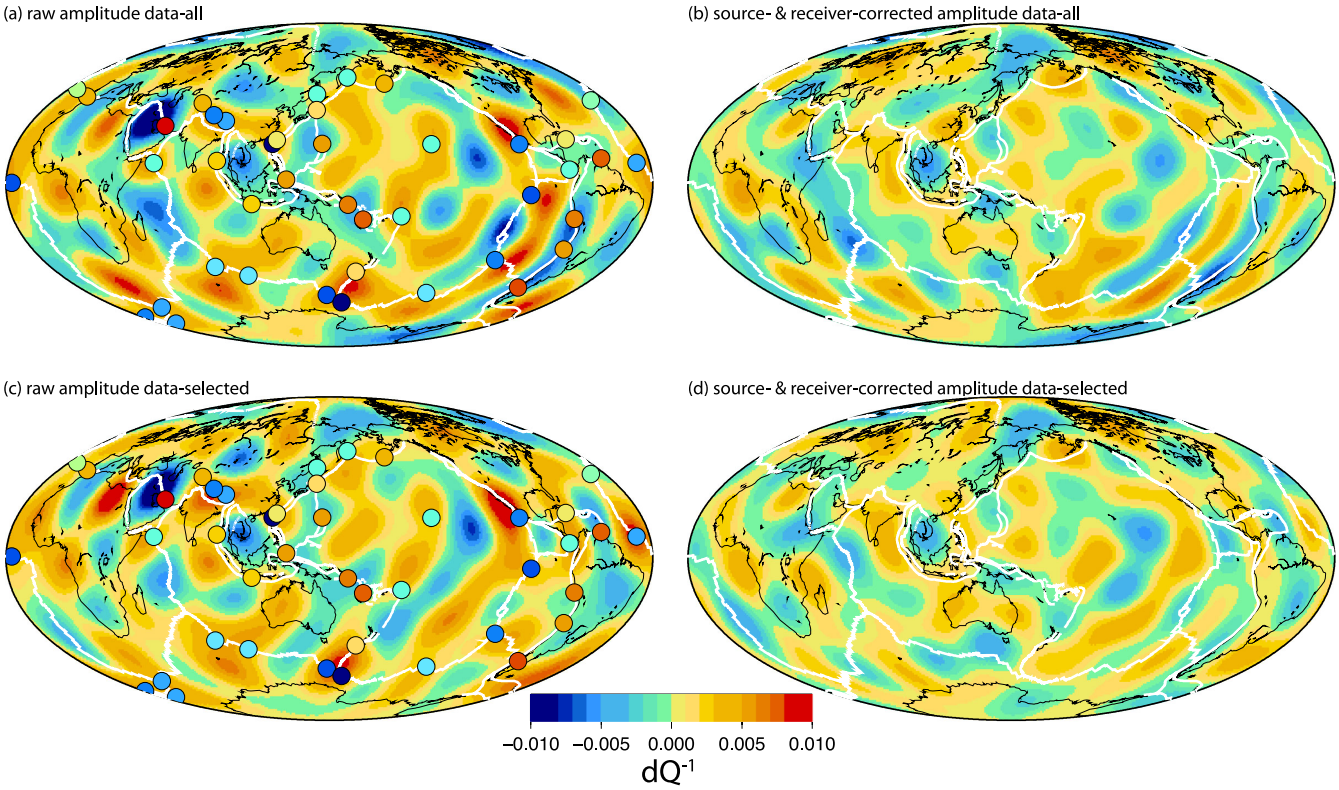

Figure 14. Attenuation maps for 50-s Rayleigh waves. (a) Amplitude measurements from 4749 paths were attributed entirely to attenuation variations. Circles show the earthquake locations, colour-coded by median event amplitude using the same scale as Fig. 5. (b) As in (a) but here the amplitude measurements have been corrected for source excitation and receiver amplitude prior to inversion. (c and d) As in (a) and (b) but for the 3234 paths selected for being oriented away from nodes in the radiation pattern.

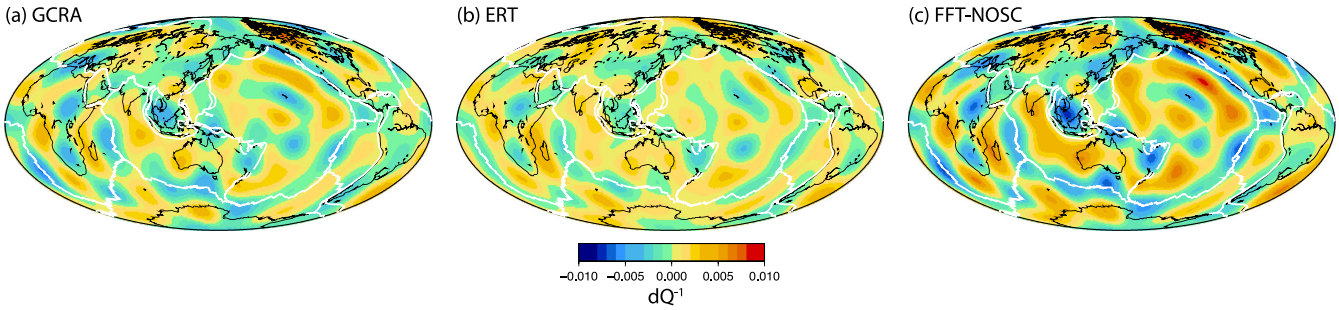

Figure 15. The attenuation maps that result when predicted amplitudes due to focusing effects are attributed entirely to attenuation variations. Calculated for 50-s Rayleigh waves for the full data set (4749 paths). (a) Amplitudes predicted using the great-circle ray approximation are inverted for attenuation. (b) Amplitudes predicted using exact ray theory are inverted for attenuation. (c) Amplitudes predicted using finite-frequency theory are inverted for attenuation.

amplitudes, perhaps because the predicted amplitude anomalies are too strong.

The amplitude of the attenuation variations in Figs 14(b) and (d) (±0.005–0.007) is somewhat smaller than the magnitude of variations observed in the true Earth. For example, the global Rayleigh-wave attenuation maps of Dalton & Ekström (2006a) contain variations of approximately ±0.007–0.01 at these periods, and Figs 14(b) and (d) therefore suggest that unmodelled path effects on amplitude, especially focusing and defocusing, can have a measurable influence on retrieved attenuation structure. To better quantify the impact of unmodelled focusing effects on attenuation structure, we have generated a synthetic data set of Rayleigh-wave amplitudes that are due to attenuation variations. Realistic attenuation maps are created by scaling the phase-velocity maps used in this study by a constant factor to achieve a realistic range of attenuation variations, truncating the maps at spherical-harmonic degree 12, and using the GCRA (eq. 11) to predict a surface wave amplitude for each path. For 50-s Rayleigh waves, we use a scaling factor of −0.0024 to convert the phase-velocity perturbations (in per cent) to perturbations in absolute attenuation, which yields an attenuation map with anomalies that vary by approximately ±0.01 (Fig. 17a). For this simple experiment, the effect of attenuation variations on amplitude is predicted with the GCRA (eq. 11). In a future study we will include 3-D attenuation variations in the computation of SPECFEM synthetics.

The amplitude anomalies due to the synthetic attenuation variations are combined with the measured amplitudes corrected for local source and receiver structure to create a data set that has sensitivity to both attenuation variations and unmodelled path effects. Fig. 17 shows a comparison of the input attenuation map and the retrieved

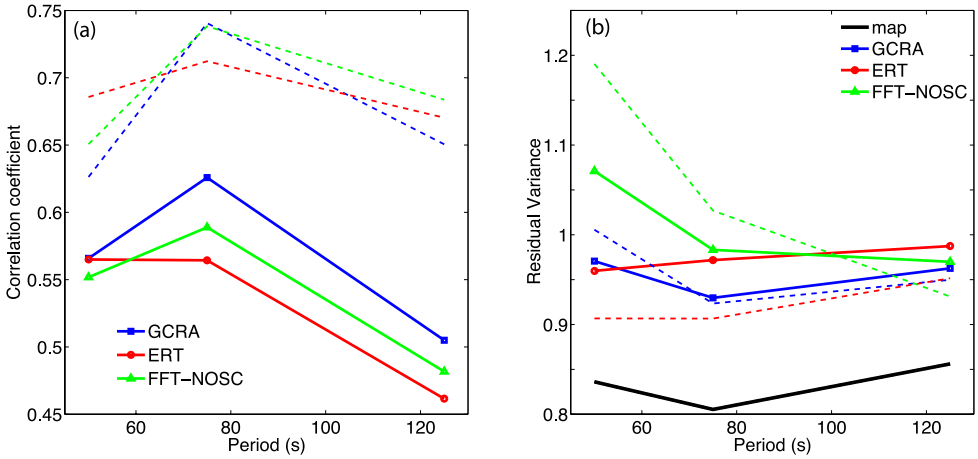

Figure 16. (a) Correlation coefficient between attenuation map determined from amplitude measurements corrected for source excitation and receiver amplitude (e.g. Figs 14b and d) and attenuation maps obtained by inverting the focusing-predicted amplitudes (e.g. Fig. 15). Solid lines with symbols are for the full data set, and dashed lines are for the selected data set. (b) Residual variance of the amplitude measurements corrected for source excitation and receiver amplitude. Variance calculations are performed using the attenuation maps determined from the focusing-predicted amplitudes (i.e. Fig. 15). Solid lines with symbols are for the full data set and dashed lines for the selected data set. Also shown in solid black is the residual variance calculated with the attenuation maps that are determined from amplitude measurements corrected for source excitation and receiver amplitude (Figs 14b and d).

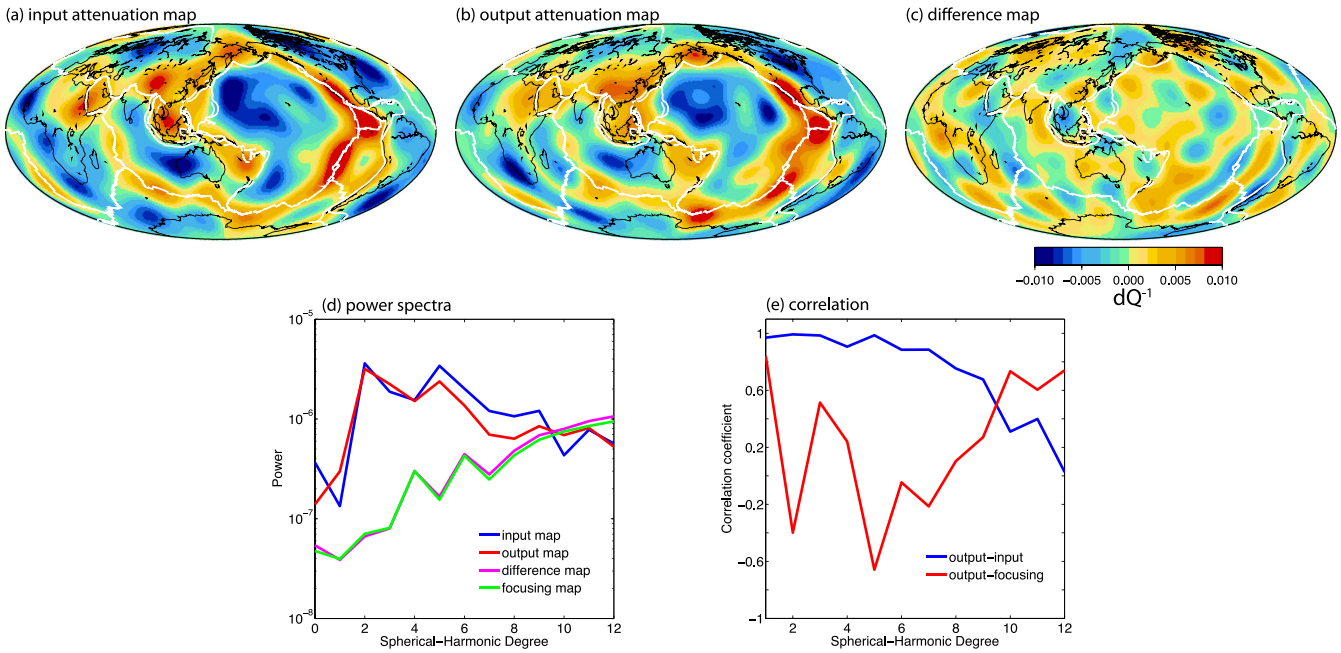

Figure 17. Effect on attenuation maps of unmodelled path effects on amplitude. For 50-s Rayleigh waves. (a) Input attenuation map, created by scaling the 50-s phase-velocity map. (b) Output attenuation map obtained by inverting an amplitude data set that has sensitivity to lateral attenuation variations and unmodelled path effects such as focusing. (c) Difference between the maps in (a) and (b). (d) Power spectra of the input, output and differenced attenuation maps. Green curve shows the power spectrum of the map in Fig. 14(b). (e) Correlation coefficient at each spherical-harmonic degree between the output attenuation map and the input map (blue) and between the output attenuation map and Fig. 14(b; red).

attenuation structure obtained from inverting the combined amplitude data set. The long-wavelength features of the input and output maps are generally similar, and differences are most pronounced at higher degrees (Fig. 17c). The attenuation maps that result from unmodelled path effects on the amplitude data (Figs 14b and d) are dominated by short-wavelength features, as is evident from their power spectra (Fig. 17d), whereas the input attenuation map has the greatest power at low degrees. As a result, the output attenuation map obtained from inverting the combined amplitude data set is very highly correlated with the input attenuation map at degrees <6, and the correlation decreases at higher degrees, which are more strongly corrupted by the unmodelled focusing effects (Fig. 17e). Similarly, the correlation between the output map and the attenuation map that results from unmodelled path effects on the amplitude data is strongest at the highest degrees, reflecting the contribution of focusing effects to the output attenuation map at high degrees. This experiment demonstrates that high-degree attenuation structure is more likely to be contaminated by focusing and scattering effects, whereas low-degree features can be imaged with greater confidence.

4.1.2 Scenario 2: imperfectly known source parameters and Earth structure

In this section, we treat the SPECFEM amplitude measurements as we would amplitude measurements made for the real Earth. We follow the approach of Dalton & Ekström (2006a) and consider each amplitude measurement to depend on four terms (eq. 6), with contributions from the source, receiver, focusing effects and attenuation. For observations of amplitude anomalies A_{ij} from source i and receiver j, we solve for an amplitude correction factor for each earthquake (A^i_S), an amplitude correction factor for each receiver (A^j_R) and the spherical-harmonic coefficients of the attenuation map q_{lm}:

$$\frac{-2U}{\omega X_{ij}}\left[\log A^i_S + \log A^j_R\right] + \sum_{l=0}^{L_{\max}} \sum_{m=-l}^{l} q_{lm}(\omega)\overline{Y^{ij}_{lm}} = \frac{-2\,U \log A_{ij}}{\omega X_{ij}}. \tag{12}$$

In eq. (12), X_{ij} is the length of the great-circle path connecting the source and receiver, $\overline{Y^{ij}_{lm}}$ is the great-circle path average of the fully normalized spherical harmonic of degree l and order m and $L_{\max}$ is the maximum degree of the expansion. A roughness-minimization constraint is applied to the spherical-harmonic coefficients. Focusing effects on amplitude A_F are not explicitly considered with this approach.

Fig. 18 shows the source and receiver correction factors that are determined from this inversion. There is good agreement between the source correction factors and the median predicted source–excitation ratios (i.e. Section 3.1; Fig. 6), suggesting that the source correction factors determined from an inversion such as this can account for the effects on amplitude of the local Earth structure at the earthquake source. The weaker agreement between the receiver correction factors and the median predicted receiver–amplitude ratio is consistent with the results of Fig. 7 and reflects the fact that the effect of the local Earth structure on receiver amplitude is smaller than it is on source amplitude. The receiver factors that Dalton & Ekström (2006a) determined in their global study spanned a larger range of values (∼0.75–1.25) than found here, but many of these factors were attributed to errors in the instrument response rather than the local Earth structure at the receiver (Ekström *et al.* 2006).

The attenuation maps determined from the inversion are presented in Figs 18(a) and (d). Because the effect of the local Earth structure at the source and receiver is accounted for by the source and receiver correction factors, and because the input earth model contains lateral variations in elastic velocity and not attenuation, the attenuation variations originate from elastic propagation effects, such as focusing and scattering, on wave amplitude. Correlation between the maps in Figs 18(a) and (d) and the attenuation maps obtained when the raw amplitude measurements have been corrected for local source and receiver structure (e.g. Fig. 14b) is 0.73, 0.77 and 0.68 at 50, 75 and 125 s. The two sets of maps are not identical in part because they are obtained from slightly different data sets; for the inversion described in this section we require each event to be recorded by >25 receivers and each receiver to record >25 events, which reduces the data set by ∼500 paths. Differences can also occur because the source and receiver factors are handled differently in the two inversions.

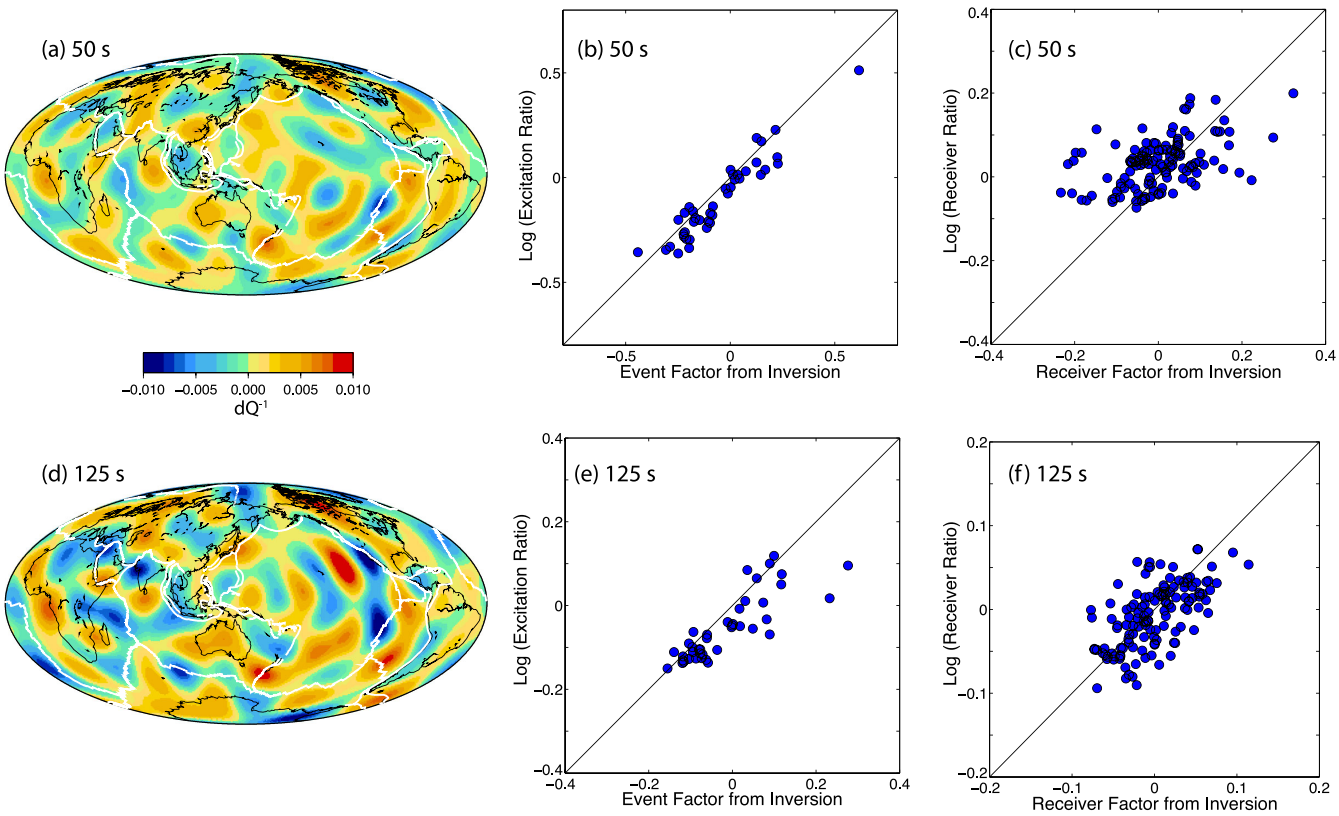

Figure 18. (a,d) The attenuation map obtained when the raw amplitude measurements are inverted for a degree-12 attenuation map and source and receiver correction factors. (b,e) Comparison of the source correction factors with the median source–excitation ratios for each event (i.e. Fig. 6). (c,f) Comparison of the receiver correction factors with the receiver–amplitude ratios for each station (i.e. Fig. 7). (a–c) For 50-s Rayleigh waves. (d–f) For 125-s Rayleigh waves.

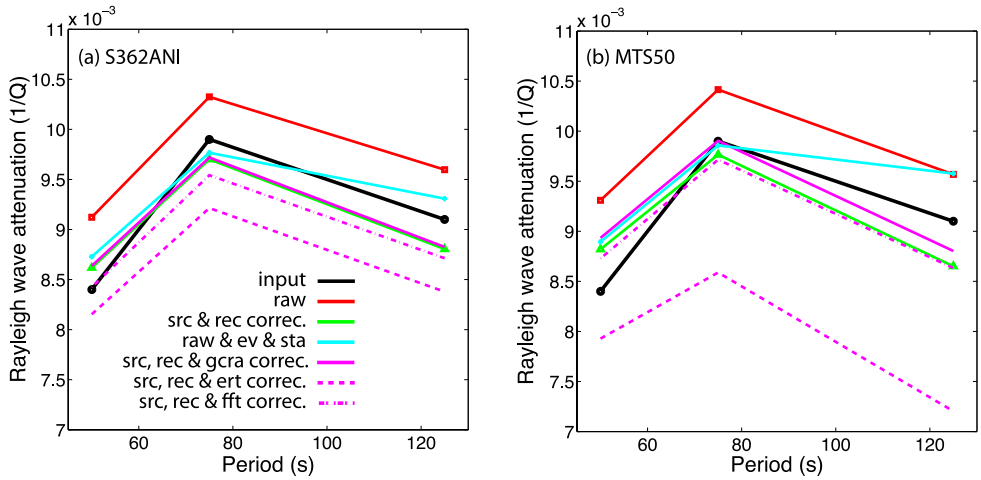

Figure 19. Globally averaged Rayleigh-wave attenuation as a function of period. The input earth model (black) is compared to the degree-0 values from various attenuation maps. 'raw' corresponds to Fig. 14(a), 'src & rec correc.' corresponds to Fig. 14(b), and 'raw & ev & sta' corresponds to Fig. 18(a). Magenta curves correspond to attenuation maps obtained when the raw amplitude measurements are corrected for source excitation, receiver amplitude and focusing effects using either GCRA, ERT or FFT-NOSC. (a) Results for S362ANI. (b) Results for MTS50.

4.2 Globally averaged attenuation

Fig. 19 explores the ability of the attenuation maps presented in Section 4.1 to recover the input 1-D attenuation model that was used to generate the SPECFEM synthetic seismograms. When source, receiver and focusing effects on amplitude are not accounted for, the raw amplitude measurements yield higher (4–9 per cent) Rayleigh-wave attenuation than the input model. This finding is consistent with the distribution of raw amplitude observations (Fig. 4), many of which have values <1; attributing these reduced amplitudes entirely to attenuation results in anomalously high attenuation. Correcting for the effects of local structure at the earthquake source removes much of this bias, and most of the inversions that account for source and receiver amplitude are characterized by average global attenuation values closer to the input model (Fig. 19). At 50 s, several of the maps contain average attenuation that is slightly higher (3–4 per cent) than the input model; at longer periods, the average attenuation is typically lower (0.5–8 per cent) than the input model.

It has been suggested that global attenuation models for the real Earth are biased towards anomalously high attenuation, perhaps by as much as 17–72 per cent in the upper mantle, because of scattering effects that divert surface wave energy away from the propagation path (Yang *et al.* 2007). The reduced surface wave amplitude that would accompany this scattering would manifest as anomalously high attenuation, since multiple scattering is typically not considered in global attenuation studies. The results shown in Fig. 19 suggest that unaccounted-for scattering effects may result in slightly higher attenuation at the highest frequencies, for which small-scale elastic heterogeneities can affect the relatively short-wavelength surface waves, but the effect on attenuation is much smaller (<5 per cent, even for the MTS50 model) than has been proposed for the Earth. Furthermore, our results show no evidence that scattering should produce anomalously high attenuation for longer period waves.

5 CONCLUSIONS

We have presented the results of a controlled experiment to investigate how assumptions and approximations in the measurement and analysis techniques for Rayleigh-wave amplitudes influence the attenuation structure that is determined through inversion of the amplitudes. Amplitudes from spectral-element synthetic seismograms are measured with respect to a reference waveform calculated for a 1-D earth model with mode summation. The source is excited in the 3-D earth model for the synthetic seismograms and in PREM for the reference waveform. This discrepancy results in large variations in the average amplitude for each event that correlate with tectonic setting, and it shifts the median amplitude measurement towards values <1. We show that the average event amplitudes are well explained by the effect of local structure on source excitation. The effect of the local Earth structure on receiver amplitude is considerably smaller than on source amplitude.

The measured amplitudes, corrected for the effects of the local Earth structure at the source and receiver, are compared to focusing effects predicted using the GCRA, ERT and FFT. For the earth models we have tested, ERT provides the best fit to the amplitudes at 50 s, and FFT is most successful at 75 and 125 s. This result indicates that the approximation of the surface wave as a thin ray that can bend according to local velocity structure, rather than as a broad kernel that is symmetric about the great-circle path, is more appropriate for the short wavelengths that characterize higher frequency surface waves. At lower frequencies, the opposite is true: the broad sensitivity zone of the surface wave cannot be ignored. We have shown that this finding depends somewhat on the source–receiver epicentral distance. It seems reasonable to hypothesize that a finite-frequency sensitivity kernel that is calculated in a 3-D earth model and is not required to be centred on the great-circle path (e.g. Yoshizawa & Kennett 2002; Zhao *et al.* 2005), which is not tested here, may provide the best fit to the amplitude data at all periods and epicentral distances.

We also investigate how the effects of elastic structure on amplitude can be mapped into erroneous attenuation variations. The effects of the local Earth structure at the earthquake source will map into large attenuation anomalies located near the events if not accounted for. When the effects of the local Earth structure at the source and receiver are accounted for, the resulting attenuation variations are strongly correlated with the maps obtained from inverting the focusing-predicted amplitudes for attenuation variations, indicating that much of the unmodelled signal in the SPECFEM amplitudes is due to focusing. When the effects on

amplitude of lateral attenuation variations and focusing are both considered, we find that the long-wavelength features of the input attenuation model are recovered while the higher degrees are more susceptible to corruption by the elastic propagation effects. Multiple scattering may lead to slight enhancement (<5 per cent) of globally averaged Rayleigh-wave attenuation at short periods, but we find no evidence of anomalously high average global attenuation at longer periods when the effects of local source and receiver structure are accounted for.

When working with surface wave amplitudes acquired on the real Earth, we do not know the local Earth structure perfectly. We have shown that the median amplitude for each event can approximate the effect of the local Earth structure on source excitation, and that local phase-velocity perturbations can approximate the effect of local structure on the receiver amplitude. Alternatively, source and receiver correction factors can be determined as part of the inverse problem (Dalton & Ekström 2006a). We note that our study did not consider errors in the instrument response, which can be large (Ekström *et al.* 2006) and, unlike the effects of the local Earth structure, cannot be approximated by phase-velocity variations. At short periods, prediction of focusing effects on amplitude is most appropriate with ERT, whereas FFT should be used at longer periods. Since surface wave phase-delay and amplitude measurements are both sensitive to elastic structure, the two data sets can be jointly inverted for elastic and anelastic models as well as amplitude correction factors for each source and receiver (e.g. Yang *et al.* 2007; Dalton *et al.* 2008).

ACKNOWLEDGEMENTS

This work was funded by National Science Foundation awards EAR-0910803 to CD and EAR-1010775 to GE and VH. The software package SPECFEM3D_GLOBE was obtained from the Computational Infrastructure for Geodynamics (geodynamics.org).

REFERENCES

Abercrombie, R.E. & Ekström, G., 2003. A reassessment of the rupture characteristics of oceanic transform earthquakes, *J. geophys. Res.,* **108,** doi:10.1029/2001JB000814.

Bassin, C., Laske, G. & Masters, G., 2000. The current limits of resolution for surface wave tomography in North America, *EOS, Trans. Am. geophys. Un.,* **81,** F897.

Boschi, L., 2006. Global multiresolution models of surface wave propagation: comparing equivalently regularized Born and ray theoretical solutions, *Geophys. J. Int.,* **167,** 238–252.

Bozdag, E. & Trampert, J., 2008. On crustal corrections in surface wave tomography, *Geophys. J. Int.,* **172,** 1066–1082.

Dahlen, F.A. & Tromp, J., 1998. *Theoretical Global Seismology,* 1025 pp, Princeton Univ. Press.

Dalton, C.A. & Ekström, G., 2006a. Global models of surface-wave attenuation, *J. geophys. Res.,* **111,** doi:10.1029/2005JB003997.

Dalton, C.A. & Ekström, G., 2006b. Constraints on global maps of phase velocity from surface-wave amplitudes, *Geophys. J. Int.,* **167,** doi:10.1111/j.1365-246X.2006.03142.x

Dalton, C.A., Ekström, G. & Dziewonski, A.M., 2008. The global attenuation structure of the upper mantle, *J. geophys. Res.,* **113,** doi:10.1029/2007JB005429.

Dalton, C.A., Ekström, G. & Dziewonski, A.M., 2009. Global seismological shear velocity and attenuation: a comparison with experimental observations, *Earth planet. Sci. Lett.,* **284,** 65–75.

Durek, J.J. & Ekström, G., 1996. A radial model of anelasticity consistent with long-period surface-wave attenuation, *Bull. seism. Soc. Am.,* **86,** 144–158.

Dziewonski, A.M. & Anderson, D.L., 1981. Preliminary reference earth model, *Phys. Earth planet. Inter.,* **25,** 297–356.

Dziewonski, A.M., Chou, T.-A. & Woodhouse, J.H., 1981. Determination of earthquake source parameters from waveform data for studies of global and regional seismicity, *J. geophys. Res.,* **86,** 2825–2852.

Ekström, G., Tromp, J. & Larson, E.W.F., 1997. Measurements and global models of surface wave propagation, *J. geophys. Res.,* **102,** 8137–8157.

Ekström, G., Dalton, C.A. & Nettles, M., 2006. Observations of time-dependent errors in the long-period instrument gain at global seismic stations, *Seism. Res. Lett.,* **77,** 12–22.

Ekström, G., Nettles, M. & Dziewonski, A.M., 2012. The global CMT project 2004–2010: centroid-moment tensors for 13,017 earthquakes, *Phys. Earth planet. Inter.,* **200–201,** 1–9.

Faul, U.H. & Jackson, I., 2005. The seismological signature of temperature and grain size variations in the upper mantle, *Earth planet. Sci. Lett.,* **234,** 119–134.

Ferreira, A.M.G. & Woodhouse, J.H., 2007. Source, path and receiver effects on seismic surface waves, *Geophys. J. Int.,* **168,** 109–132.

Gung, Y. & Romanowicz, B., 2004. Q tomography of the upper mantle using three component long period waveforms, *Geophys. J. Int.,* **157,** 813–830.

Hammond, W.C. & Humphreys, E.D., 2000. Upper mantle seismic wave attenuation: effects of realistic partial melt distribution, *J. geophys. Res.,* **105,** 10 987–10 999.

Jordan, T.H., 1981. Global tectonic regionalization for seismological data analysis, *Bull. seism. Soc. Am.,* **71,** 1131–1141.

Karato, S., 2003. Mapping water content in the upper mantle, in *Inside the Subduction Factory,* Vol. 138, pp. 135–152, AGU Geophysical Monograph.

Komatitsch, D. & Tromp, J., 2002a. Spectral-element simulations of global seismic wave propagation: I. Validation, *Geophys. J. Int.,* **149,** 390–412.

Komatitsch, D. & Tromp, J., 2002b. Spectral-element simulations of global seismic wave propagation: I. Three-dimensional models, oceans, rotation and self-gravitation, *Geophys. J. Int.,* **150,** 303–318.

Kustowski, B., Ekström, G. & Dziewonski, A.M., 2008. The anisotropic shear-wave velocity structure of the Earth's mantle: a global model, *J. geophys. Res.,* **113,** doi:10.1029/2007JB005169.

Larson, E.W.F., Tromp, J. & Ekström, G., 1998. Effects of slight anisotropy on surface waves, *Geophys. J. Int.,* **132,** 654–666.

Lee, C-T.A., 2003. Compositional variation of density and seismic velocities in natural peridotites at STP conditions: implications for seismic imaging of compositional heterogeneities in the upper mantle, *J. geophys. Res.,* **108,** doi:10.1029/2003JB002413.

Lekic, V. & Romanowicz, B., 2011. Inferring upper mantle structure by full waveform tomography using the spectral element method, *Geophys. J. Int.,* **185,** 799–831.

Mitchell, B.J., 1995. Anelastic structure and evolution of the continental crust and upper mantle from seismic surface wave attenuation, *Rev. Geophys.,* **33,** 441–462.

Nataf, H.-C. & Ricard, Y., 1996. 3SMAC: an a priori tomographic model of the upper mantle based on geophysical modeling, *Phys. Earth planet. Inter.,* **95,** 101–122.

Nettles, M. & Dziewonski, A.M., 2011. Effect of higher-mode interference on measurements and models of fundamental-mode surface-wave dispersion, *Bull. seism. Soc. Am.,* **101,** 2270–2280.

Ritsema, J., Deuss, A., van Heijst, H.J. & Woodhouse, J.H., 2011. S40RTS: a degree-40 shear-velocity model for the mantle from new Rayleigh wave dispersion, teleseismic traveltimes, and normal-mode splitting function measurements, *Geophys. J. Int.,* **184,** 1223–1236.

Ritzwoller, M.H., Shapiro, N.M., Barmin, M.P. & Levshin, A.L., 2002. Global surface wave diffraction tomography, *J. geophys. Res.,* **107,** doi:10.1029/2002JB001777.

Romanowicz, B., 1995. A global tomographic model of shear attenuation in the upper mantle, *J. geophys. Res.,* **100,** 12 375–12 394.

Roth, E.G., Wiens, D.A. & Zhao, D., 2000. An empirical relationship between seismic attenuation and velocity anomalies in the upper mantle, *Geophys. Res. Lett.,* **27,** 601–604.

Selby, N.D. & Woodhouse, J.H., 2000. Controls on Rayleigh wave amplitudes: attenuation and focusing, *Geophys. J. Int.,* **142,** 933–940.

Selby, N.D. & Woodhouse, J.H., 2002. The Q structure of the upper mantle: constraints from Rayleigh wave amplitudes, *J. geophys. Res.,* **107,** doi:10.1029/2001JB000257.

Spetzler, J., Trampert, J. & Sneider, R., 2002. The effect of scattering in surface wave tomography, *Geophys. J. Int.,* **149,** 755–767.

Tromp, J. & Dahlen, F.A., 1992. Variational principles for surface wave propagation on a laterally heterogeneous Earth—II. Frequency-domain JWKB theory, *Geophys. J. Int.,* **109,** 599–619.

Wang, Z. & Dahlen, F.A., 1994. JWKB surface-wave seismograms on a laterally heterogeneous Earth, *Geophys. J. Int.,* **119,** 381–401.

Wang, Z. & Dahlen, F.A., 1995. Validity of surface-wave ray theory on a laterally heterogeneous Earth, *Geophys. J. Int.,* **123,** 757–773.

Woodhouse, J.H. & Wong, Y.K., 1986. Amplitude, phase and path anomalies of mantle waves, *Geophys. J. R. astr. Soc.,* **87,** 753–773.

Yang, Y. & Forsyth, D.W., 2006. Regional tomographic inversion of amplitude and phase of Rayleigh waves with 2-D sensitivity kernels, *Geophys. J. Int.,* **166,** 1148–1160.

Yang, Y., Forsyth, D.W. & Weeraratne, D.S., 2007. Seismic attenuation near the East Pacific Rise and the origin of the low-velocity zone, *Earth planet. Sci. Lett.,* **258,** 260–268.

Yoshizawa, K. & Ekström, G., 2010. Automated multi-mode phase speed measurements for high-resolution regional-scale tomography: application to North America, *Geophys. J. Int.,* **183,** 1538–1558.

Yoshizawa, K. & Kennett, B.L.N., 2002. Determination of the influence zone for surface wave paths, *Geophys. J. Int.,* **149,** 440–453.

Yoshizawa, K. & Kennett, B.L.N., 2004. Multimode surface wave tomography for the Australian region using a three-stage approach incorporating finite frequency effects, *J. geophys. Res.,* **109,** doi:10.1029/2002JB002254.

Zhao, L., Jordan, T.H., Olsen, K.B. & Chen, P., 2005. Frechet kernels for imaging regional Earth structure based on three-dimensional reference models, *Bull. seism. Soc. Am.,* **95,** 2066–2080.

Zhou, Y., Dahlen, F.A. & Nolet, G., 2004. Three-dimensional sensitivity kernels for surface wave observables, *Geophys. J. Int.,* **158,** 142–168.

Zhou, Y., Dahlen, F.A., Nolet, G. & Laske, G., 2005. Finite-frequency effects in global surface-wave tomography, *Geophys. J. Int.,* **163,** 1087–1111.